

Papers Presented at the

15th

Annual

Summer Intern Conference

August 12, 1999

Houston, Texas

QB
501
P374
1999

1999 Summer Intern Program for Undergraduates
Lunar and Planetary Institute

Papers Presented at the

Fifteenth Annual
SUMMER INTERN CONFERENCE

August 12, 1999
Houston, Texas

1999 Summer Intern Program for Undergraduates
Lunar and Planetary Institute

Sponsored by
Lunar and Planetary Institute
NASA Johnson Space Center

CIRS/LIBRARY
LUNAR AND PLANETARY INSTITUTE
3600 BAY AREA BOULEVARD
HOUSTON TX 77058-1113

Compiled in 1999 by

Publications and Program Services Department
Lunar and Planetary Institute
3600 Bay Area Boulevard
Houston TX 77058-1113, USA

Material in this volume may be copied without restraint for library, abstract service, education, or personal research purposes; however, republication of any paper or portion thereof requires the written permission of the authors as well as appropriate acknowledgment of this publication.

The Lunar and Planetary Institute is operated by the Universities Space Research Association under Contract No. NASW-4574 with the National Aeronautics and Space Administration.

THE LUNAR AND PLANETARY INSTITUTE
3600 BAY AREA BOULEVARD
HOUSTON, TEXAS 77058-1113
(713) 289-2700

FIFTEENTH ANNUAL SUMMER INTERN CONFERENCE PROGRAM

AUGUST 12, 1999—LPI LECTURE HALL

Morning Session *Chair: Paul D. Spudis*

- 9:00 a.m. **CARRIE M. ANDERSON-MUNFORD** Advisor: Andrew E. Potter
The Analysis of Sodium and Potassium in the Mercurian Exosphere
- 9:20 a.m. **JOSEF DUFEK** Advisor: Robert Herrick
Evolution of Large Shield Volcanoes on Venus
- 9:40 a.m. **COLIN GRIFFIN** Advisors: Carlton Allen and Eileen Stansbery
Techniques to Evaluate Microbial Contamination
- 10:00 a.m. **Break**
- 10:15 a.m. **EMMA-KATE POTTER** Advisor: Walter Kiefer
The Thermal Structure of Venus: A Flexural Analysis
- 10:35 a.m. **DANIELLE E. ROSE** Advisor: Paul D. Spudis
Piercing the Clouds: Stratigraphy of Mare Nubium
- 10:55 a.m. **STEVEN SOBIESZCZYK** Advisor: Paul Schenk
Mapping the Impact Crater Asymmetry on Ganymede
- 11:15 a.m. **Lunch**

Afternoon Session
Chair: Friedrich P. Hörz

- 1:00 p.m. **LORA VARLEY** Advisor: Friedrich Hörz
*The Modal Composition of the Kaibab Formation at
Meteor Crater, AZ*
- 1:20 p.m. **JENNIFER A. WAGGONER** Advisor: Allan H. Treiman
*Sedimentary Deposits in Gangis Chasma, Mars: Stereo and
Geomorphic Analysis*
- 1:40 p.m. **DANIELLE L. WILHELMI** Advisors: David C. Black and Tomasz F. Stepinski
*The Search for Extrasolar Planets: A New Approach Using a
Genetic Algorithm*
- 2:00 p.m. **Adjourn**

CONTENTS

The Analysis of Sodium and Potassium in the Mercurian Exosphere <i>Carrie M. Anderson-Munford</i>	1
Evolution of Large Shield Volcanoes on Venus <i>Josef Dufek</i>	4
Techniques to Evaluate Microbial Contamination <i>Colin Griffin</i>	7
The Thermal Structure of Venus: A Flexural Analysis <i>Emma-Kate Potter</i>	10
Piercing the Clouds: Stratigraphy of Mare Nubium <i>Danielle E. Rose</i>	13
Mapping the Impact Crater Asymmetry on Ganymede <i>Steven Sobieszczyk</i>	16
The Modal Composition of the Kaibab Formation at Meteor Crater, AZ <i>Lora Varley</i>	19
Sedimentary Deposits in Gangis Chasma, Mars: Stereo and Geomorphic Analysis <i>Jennifer A. Waggoner</i>	22
The Search for Extrasolar Planets: A New Approach Using a Genetic Algorithm <i>Danielle L. Wilhelmi</i>	25

The Analysis of Sodium and Potassium in the Mercurian Exosphere

Carrie M. Anderson-Munford, Arizona State University, Tempe, AZ

Advisor: Dr. Andrew E. Potter, Lunar and Planetary Institute, Houston, TX

I. Introduction

Sodium (Na) and Potassium (K) atoms can be seen in the exosphere of Mercury and the Moon because they are extremely efficient at scattering sunlight. The concentration of sodium and potassium atoms can be determined from the intensity of the scattered light. Sodium and potassium are found to have extremely low concentrations. On Mercury, the column densities are for Na $\approx 10^{11}$ atoms cm^{-2} and K $\approx 10^9$ atoms cm^{-2} [1], and on the Moon, $3 \times 10^8 < \text{Na} < 3 \times 10^9$ atoms cm^{-2} and $3 \times 10^7 < \text{K} < 3 \times 10^8$ atoms cm^{-2} [2]. We believe that the sodium and potassium atoms are produced from surface rocks, by some form of sputtering, although meteoroid material may also contribute. For that reason, it is not surprising to find the ratio of Na/K in the Moon's exosphere to be ≈ 7 -8, which is similar to the ratio in the bulk composition of the moon [3]. We might expect a similar ratio of Na/K in Mercury's exosphere, but this is not the case. Past observations found the ratio to be between 80 [4] and 100 [1], when the measurement was made near solar minimum, and ~ 190 [4], when the measurement was made near solar maximum. It seems unreasonable that such a high ratio represents the ratio in the surface rocks. Based on lunar samples and from meteoritic samples where the ratio of Na/K ~ 13 [3], the ratio of the sputtered Na/K should theoretically be less than 22 and greater than 7. The high ratio suggests that potassium is being lost from mercury at a greater rate than sodium. Solar photoionization is the main candidate for this loss process, followed by the capture of ions by the solar wind. This is one reason that a correlation between the ratio and solar activity might exist.

The purpose of this paper is to describe the work performed in analyzing a collection of Na and K data and to look into any correlation relating to solar activity.

II. Procedure

Sodium and potassium scatter light extremely efficiently at their D₁ and D₂ resonance wavelengths. For sodium, the D₁ line scatters at 5896Å and the D₂ line scatters at 5890Å. For potassium, the D₁ line scatters at 7699Å and the D₂ line scatters at 7664Å. Usually, the molecular oxygen in the Earth's atmosphere obscures the potassium D₂ line. A few times a year when the Mercury-Earth Doppler shift is large enough, the potassium D₂ Fraunhofer line completely shifts out from under the oxygen Fraunhofer line.

When sodium and potassium atoms are at rest relative to the Sun, they scatter light efficiently but only see low solar intensities at the bottom of the deep Na and K Fraunhofer lines, about 5% of the solar continuum. When Mercury and the sodium and potassium atoms in its atmosphere are moving rapidly relative to the Sun, the Fraunhofer lines shift. The result of the Doppler shift increases the solar intensity at the sodium and potassium resonance wavelengths. The atoms see more light and hence scatter more light. When the emission lines are near continuum level, the scattered light intensity is greatest and extractions of sodium and potassium emission lines are possible. Heliocentric velocity data [5] was used to determine relevant Sun-Mercury Doppler shifts and large potassium Doppler shifts were selected around $\pm 250 \text{ mÅ}$.

The Image Reduction and Analysis Facility (IRAF) program was used to analyze the raw spectra of Mercury. The sodium and potassium emission signals were extracted and calibrated so that ratios of sodium and potassium were deduced. In order to calculate Na/K, the Na and K column densities in atoms cm^{-2} were determined. The column densities were calculated from the sodium and potassium emission intensities (Rayleighs, photons/ cm^2

Anderson-Munford: Mercury's exosphere

column/s) and from the number of photons that each sodium and potassium atom scatter per second per square distance (g') [6]. The next step was to estimate the noise in the spectra. The rms deviation of the spectrum continuum in a region free of Fraunhofer lines was computed and used as the basis for the noise calculations. This noise to signal value was used to determine the relevant error bars. Most of the error resulted from the K measurements because the K D lines are weaker than the Na D lines and they are harder to observe. The Na signal was very strong and errors were small.

III. Results

We expected sodium and potassium to correlate with solar activity. As a measure of solar activity, we chose the 10.7 cm radio flux. Previously, Shemansky and Morgan found a strong correlation between solar flux and potassium column abundance [7]. As seen in figure 1, there is no evidence to support any correlation between the two, nor between Na/K and solar flux, as seen in figure 2. Varying solar flux levels were chosen, including solar minimum and solar maximum, but no relation was detected. The Na and K column densities and solar flux values are compared in table 1.

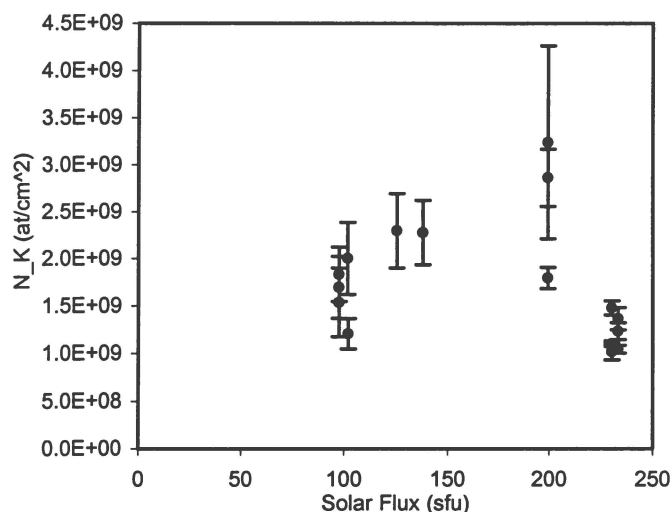


Fig. 1. The potassium column density and solar flux are compared in this figure.

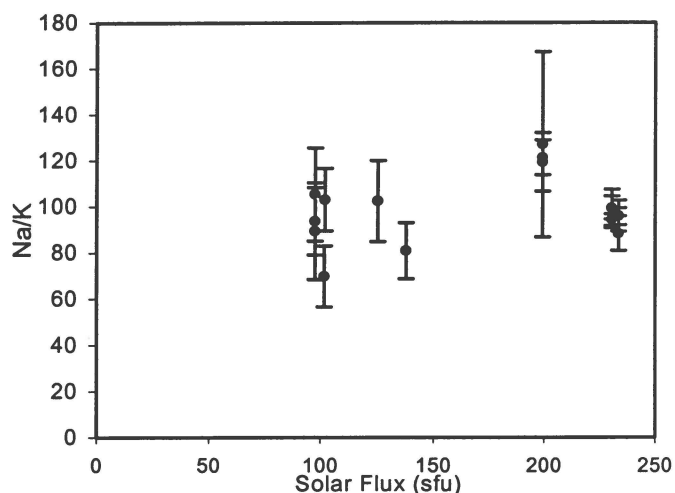


Fig. 2. The ratio of sodium-potassium and solar flux are compared in this figure.

Table 1. Na-K column density and solar flux

Date	Na density (atoms cm^{-2} column)	K density (atoms cm^{-2} column)	10.7 radio flux (sfu)
11-Jan-88	1.40E+11	2.01E+09	101.7
4-Dec-90	4.11E+11	3.24E+09	199.3
9-Dec-90	1.04E+11	1.10E+09	230.3
10-Dec-90	1.21E+11	1.37E+09	233.4
29-May-98	1.38E+11	1.54E+09	97.6
24-Apr-99	1.25E+11	1.21E+09	102
30-Apr-99	2.35E+11	2.30E+09	125.3
2-May-99	1.84E+11	2.28E+09	137.9

However, there does exist a direct correlation between the sodium emission and potassium emission intensities and number densities, as seen in figures 3 and 4. Figure 4 shows the correlation between Na-K column densities, with the trendline forced through the origin. A good fit results. The ratio of Na/K determined from this plot is 107.3.

IV. Discussion

Since sodium and potassium are physically and chemically similar, our result suggests that the origin or source processes for sodium and potassium are one in the same, which leaves uncertainties regarding the sink processes. The source processes include diffusion, impact vaporization, photosputtering, and ionsputtering.

Anderson-Munford: Mercury's exosphere

The sink processes are photoionization and solar radiation pressure.

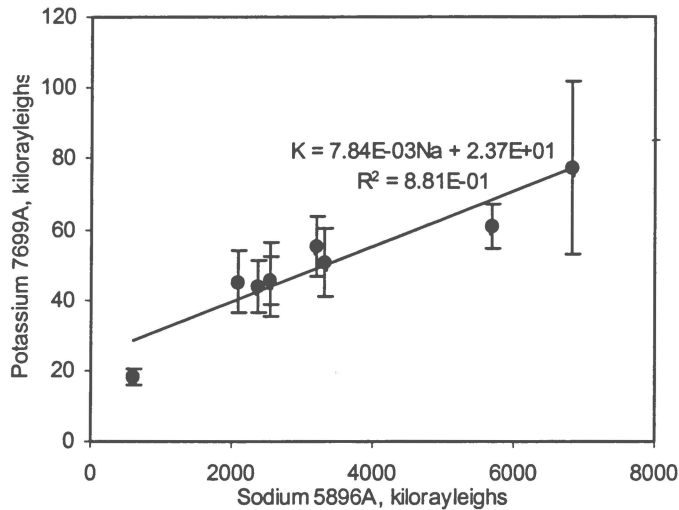


Fig. 3. Comparison of potassium and sodium intensities.

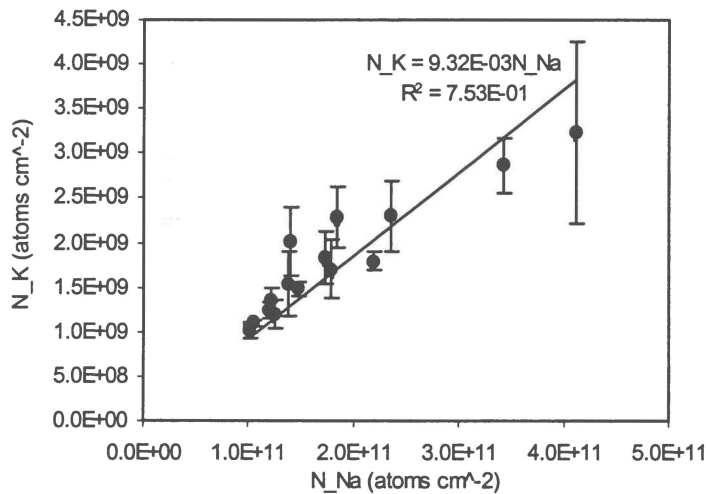


Fig. 4. Comparison of sodium and potassium column densities.

The process of radiation pressure exerts a force on the sodium and potassium atoms in Mercury's exosphere. The radiation pressure can reach values of 40% of surface gravity. The force exerted by photons will accelerate the sodium and potassium atoms that are high enough, and they will be swept entirely off the

planet. The maximum radiation pressure for potassium is larger than for sodium, where potassium atoms with velocities of 1.5 km/s can be swept away, compared to 2.1 km/s for sodium [8]. The other sink process, photoionization, involves ionization by solar UV photons. The ions can be swept off the planet by the solar wind, ejected into the Mercury magnetosphere, and can return to the surface and neutralize, which is referred to as ion recycling. Not only is potassium heavier than sodium, but potassium also ionizes easier. The photoionization rate is 40% larger for potassium than for sodium [4]. Assuming that atomic weight directly correlates with atomic mass, then once the atoms are caught up in Mercury's magnetic field, potassium will have a larger gyroradius than sodium. Rosemary Killen has suggested that since potassium already has a larger gyroradius than sodium, it will be easier for accelerated potassium to escape [9]. Even though there was no correlation found between Na-K column density and solar activity, there exists some differences between the two that might explain the large Na/K observed values. Potassium has a greater radiation pressure acceleration than sodium, which results in a larger potassium extended exosphere [8], neutral potassium has a larger photoionization rate than neutral sodium, and ionized potassium has a larger gyroradius than ionized sodium.

IV. References

- [1] Vilas, Faith. et al. *Mercury*. The University of Arizona Press: Tucson, 1988.
- [2] Hunten, D.M. and A.L. *Advances in Space Research*, 19, 1551-1559, 1997.
- [3] Lodders, Katharina and Bruce Fegley, Jr. 1998. *The Planetary Scientist's Companion*. (New York: Oxford Academy Press).
- [4] Potter, A.E. and T.H. Morgan, *Planet. Space Sci.*, 45, 95-100, 1997.
- [5] <http://ssd.jpl.nasa.gov/cgi-bin/eph>
- [6] Chamberlain, Joseph, W. 1961. *Physics of the Aurora and Airglow*. (New York and London: Academic Press).
- [7] Shemansky, D.E. and T.H. Morgan, *Geophysical Research Letters*, 18, 1659-1662, 1991.
- [8] Potter, A.E. and T.H. Morgan, *ICARUS*, 67, 336-340, 1986.
- [9] Killen, Rosemary M. Unpublished.

Evolution of Large Shield Volcanoes on Venus

Josef Dufek, University of Chicago [jddufek@midway.uchicago.edu]
Robert Herrick (advisor), Lunar and Planetary Institute, Houston TX

The ubiquitous presence of volcanism on Venus has been apparent since radar images were collected by the Russian Venera missions [1]. Subsequently, Magellan has provided higher resolution synthetic aperture radar (SAR) images, gravity data and altimetry data. This data has further fostered the discussion of volcanism and the resulting implications regarding the history of both surficial and deep processes on Venus. The current study examines a subset of large shield volcanoes to determine if an evolutionary trend occurs from dome-shaped to central-depression morphology. Twenty volcanoes have been examined to determine their geologic history, morphology, and gravity signals. Of the volcanoes exhibiting domical morphology, 45% have features that postdated their flows. However, 100% of the central-depression volcanoes exhibit postdating features. Also, the domical group has an average isostatic gravity anomaly of 22mGals. Such a large positive anomaly can be interpreted as the presence of dynamic support. Those volcanoes with central depressions lack this large positive anomaly with an average of -75mGals. They are interpreted to be supported by Airy type isostasy. The similarity in appearance and size of the volcanoes examined justifies categorization of the group into a single class of phenomena. Furthermore, the marked difference in age linked to a central-depression morphology suggests that a large collapse of the central region is linked to a general evolutionary trend in volcanoes that have lost dynamic support.

Introduction: Initial studies by Herrick and Marsh [2] of Kunhild and Ereshkigal, two large volcanoes on Venus, indicated that these two features are examples of extinct volcanoes. These volcanoes appear similar to other large volcanoes on Venus in the SAR imagery and exhibit characteristic radial flows. However, both volcanoes have large central depressions (150km and 350km in diameter for Kunhild and Ereshkigal, respectively) that were interpreted to result from the removal of dynamic support. They also noted the presence of a postdating crater on the flows of Kunhild and postdating wrinkle ridges on the flows, implying that the volcanoes have not been active for some time. To test the hypothesis that central depression formation is the final stage in the evolution of large shield volcanoes, a group of 29 volcanoes that appear superficially similar in SAR imagery was selected for further examination [2]. The purpose of this study is to delineate the geologic history of these volcanoes on Venus to examine possible age differences between those volcanoes exhibiting large central depressions and those with more domical profiles.

Procedure: Magellan data was utilized to document features unrelated to volcanic development that postdated the activity of the volcano. Three major classes of postdating features were noted. The first group includes craters located on a volcano's flows that have intact ejecta blankets and crater floors that give bright radar returns. A recent study indicates that craters on Venus with radar-dark floors have experienced lava flooding of their floors, and these craters were not considered to be a postdating features [3]. In a couple of instances, craters that postdated tectonic fractures or ridges, which in turn postdated a volcano's flows, were also counted as postdating crater events. Embayment relationships with surrounding volcanic features were also used to place a volcano in the context of the local stratigraphic column. This process was often complicated by indistinct flows. When there was a question as to the age relationship of flows, no embayment relationship was counted. Postdating tectonic deformation was noted and divided into three categories: lineaments, fractures and wrinkle ridges.

To augment the study, north-south and west-east topography profiles were made of each volcano

using Magellan nadir-looking radar altimetry (footprint 10-30km in diameter [4]). These profiles were used to divide the volcanoes into three morphometric categories. Those with central depressions with widths greater than 100km and surrounded by an annular rim were placed in a central depression category. Volcanoes with central depressions, but with volcanic edifices inside the annular rim that filled the majority of the depression, were listed as resurgent features. The rest of the volcanoes had a roughly domical shape, although there was some variability concerning summit features such as the presence of smaller caldera features. The topographic profiles were also utilized to determine the maximum height relative to the surrounding terrain, the width at half the maximum height, and the width at .5km above the base. The .5km above the base measurements were made on each profile and then averaged. If for instance there was a difference in the basal level in the north and south then the average was taken as the base marker and the .5km was measured from this point. This measurement was intended to allow a scale comparison between all features in the study.

Gravity measurements were also made across each volcano. Profiles of the geoid and isostatic gravity anomaly were made for each north-south and west-east profile. The isostatic anomaly was computed by taking the free-air gravity and subtracting the gravity signal attributed to the topography of the volcano and the negative of the topography at a compensation depth of 30km. (Density was assumed to be 2900kg/m³ and the 30km compensation depth is based on estimates of the crustal thickness[5].) Hence, a small or negative isostatic anomaly corresponds to the interpretation that the volcano can be completely supported by Airy type isostasy. A large positive isostatic anomaly most likely corresponds to some measure of dynamic support, i.e. supported by mantle upwelling. The isostatic anomaly was recorded over the center point of each volcano.

Results: The results have been tabulated in Table 1 which lists the morphometric classifications as D for domical, C for central depression, and R for resurgent feature. The category listed as Anomaly Correlation specifies whether the shape of the isostatic anomaly profile corresponds to the presence of the volcano (Y), or if it is dominated by other factors (N).

The category Postdating Features has the sub-categories for craters, and E for embayment by flows. F for fractures, L for lineaments, R for wrinkle ridges, C

Table 1-Description of Volcanoes Studied

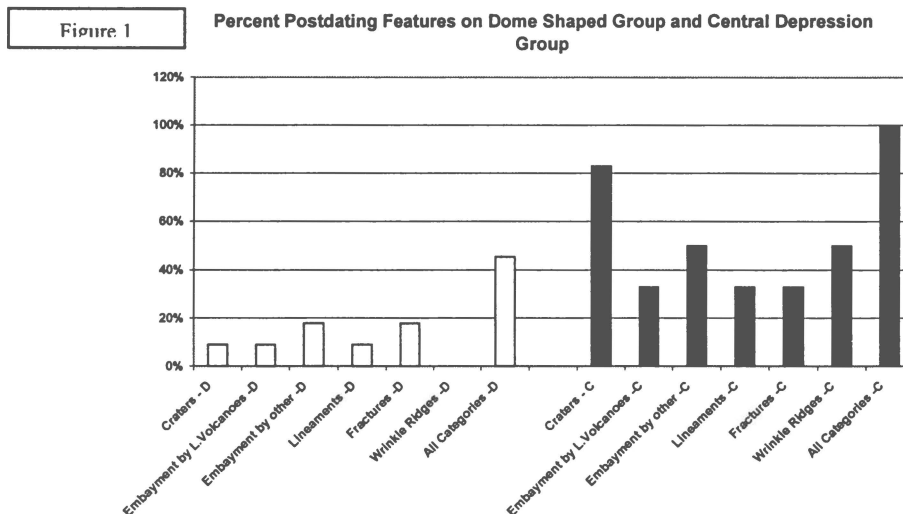
Name:	Lat.	Long.	Group	Isostatic Anom. (mGals)	Anomaly Correlation **	Height (km)	Half-Width (km)	.5km width (km)	Post-Dating Features
Api Mons	38.5	55.0	D	3	N	1.75	200	241.5	
Unnamed	2.5	45.5	D	25	Y	1.75	137.5	155	
Ushas Mons	-25.0	323.5	D	60	Y	2.0	212.5	225	L
Tepev Mons	29.5	45.5	D	45	Y	5.0	137.5	187.5	
Innini Mons	-34.5	328.0	D	28	Y	2.25	180	250	
Hathor Mons	-39.0	325.5	D	28	Y	2.25	287.5	350	
Tuulikki Mons	10.0	274.5	D	-26	N	2.0	225	275	E
Dzalarhons Mons	0	34.0	D	45	Y	3.0	112.5	200	
Sif Mons	22.0	352.0	D	46	Y	2.5	125	175	E
Uretseti Mons *	-12.5	261.5	D	0	N	2.25	125	141.5	E,F
Kunapipi Mons *	-34.0	86.0	D	-12	N	2.5	200	308	C,F
Kokyanwuti Mons	35.5	211.5	C	2.5	N	1.25	200	250	C,E,F
Itanua Corona	19.5	154.0	C	18	N	.75	200	162.5	E, C, R
Uti Hiata	16.0	69.0	C	-5	N	1.75	262.5	287.5	E, F
Nzambi Corona	-45.5	287.0	C	2	N	.7	200	187.5	C,E,R,L
Kunhild	19.0	80.0	C	-10	N	1.5	250	400	C,R
Mielikki Mons	-28.0	281.0	C	-12	N	1.5	300	300	C, L, E
Nyx Mons	30.0	49.0	R	65	Y	1.25	400	500	E
Atanua Mons	9.5	308.5	R	-11	N	1.5	275	275	
Nagavonyi Corona	-18.0	259.0	R	5	Y	.75	200	175	F

Uretseti and Kunapipi have been listed with (*) to note that these two features may have been effected by the presence of nearby rifting. Uretseti appears to have been postdated by some significant rifting on the Rabie Chasma, and Kunapipi may have had a side collapse event into Juno Chasma. The possible Kunapipi collapse appears to be a rarity on Venus for most indications point to basal welding of volcanoes to the lithosphere [10].

Eleven of the twenty volcanoes were placed in the domical category, six in the central depression category, and three in the resurgent category. In the domical category 22mGals was the average isostatic anomaly, and 7 of the 11 features had isostatic anomalies above 20mGals. Tuulikki Mons had the lowest isostatic anomaly of the group with -26mGals, which appeared extremely anomalous compared to the others in the domical group. Tuulikki also appeared to

have a visible flexural moat, which is also a rarity on Venus because most moats are thought to have been filled with lava flows [6]. The mean isostatic anomaly for the collapsed central region volcanoes was -.75mGals. With only 3 resurgent features that display varied behavior their average is of only limited validity.

Figure 1 displays the percent of volcanoes in each group that has experienced postdating events. As



can be seen, 45% of the volcanoes in the domical group had at least one postdating event, although many only had one postdating event counted on their slopes. In contrast, all of the central depression group have experienced some degree of postdating phenomena, and many are postdated by multiple events.

Characterization of Volcanoes: The volcanoes in this study had predominately radial flows, varying from sheet-like, to lobate, to digitate in appearance. In both the domical and collapsed central region volcanoes, the earliest flow units discerned were usually dark and sheet-like in SAR imagery. The mean width measured at .5km height was undertaken because at this height there would be no effect of the central depression on the width of any of the features. The mean width measured at .5km height for the dome-shaped volcanoes was 228.0km with a standard deviation of 65.0km. The same measurement on the collapsed central feature yielded a mean of 264.6km with a standard deviation as 85.7km. The similarity of scale and flow structure between these two groups allows us to draw the inference that they are related features.

Characterization of Central Depressions: The mean width of the central depressions was 137.5km with a standard deviation of 19.4km. The mean maximum depth of the depressions was .61km with the smallest maximum depth being .4km and the largest .75km. Five of the six volcanoes with central depressions had visible edifices in their interiors or on their rims. Likewise the same five volcanoes had some visible flows that embay the depressed region. Four volcanoes had concentric lineaments surrounding the interior of the depressed region and three had radial lineaments visible on their rims.

Resurgent features had volcanic edifices which dominated the central depression. The average width of these edifices is 169.33km with the smallest edifice being 125km in diameter. The resurgent features had varied gravity signals, and two of the three had postdating features. With such a small group it is difficult to be certain of any trends. The resurgent features were of similar scale and had similar flow structures as the other volcanoes studied.

Conclusions: The similarity in appearance, the .5km-width similarities, and the similarities in flow structure and flow scale justifies the assertion that the depressed central region volcanoes and the domical volcanoes are genetically related. Large shield volcanoes are thought to be directly linked to mantle upwelling on Venus[7]. The large positive isostatic anomalies over the domical volcanoes along with their relative lack of postdating features indicates

these volcanoes may still be located over mantle upwelling. The central depression volcanoes presumably formed from similar scale mantle upwelling, but as a family these volcanoes appear to have been inactive for an extended period due to the large number of postdating features. Furthermore, the gravity signals above the central depression volcanoes indicate that, as a class, they appear to be supported by Airy isostasy without significant amount of dynamic support. The central depression volcanoes, therefore, appear to be endmembers of the class of large shield volcanoes who have been cut-off from the dynamic support of mantle upwelling.

The formation of the central depressions can be compared to the modeled formation of coronae on Venus. Many coronae observed on Venus have a raised rim and an interior central depression [8]. Squyres, et al. outlined a three step process for the formation of coronae: rising mantle diapirs are thought to dome the crust, then the diaper flattens as it nears the crust creating a plateau shaped feature, finally gravitational relaxation produces a central depression [9]. For the volcanoes in our study, the presence of lineaments surrounding the central depression that postdate the major flows of the volcano is consistent with the depression forming after the active stage of the volcano. Once mantle upwelling is removed from beneath the volcano, the volcano ceases to emit major flows, the central region collapses, and the volcano lapses into a steady-state isostatic balance with compensation from a low-density root. The picture is somewhat complicated by the presence of small edifices in the depressed central regions that have produced some flows which embay the rim. Resurgent features may be the result of reestablishment of mantle upwelling in the area. The similarities between the formation of coronae and large central depressions on shield volcanoes, suggests these two features may be more related than was earlier noted, and the formation of one or the other may be related to the intensity of mantle upwelling and the flow regime in the mantle [2].

References: [1] Head J.W. et al. (1992) JGR, 97, 13,153-13198. [2] Herrick R.R. and Marsh C.A. (1997) Lunar and Planetary Sci. Conf. 28,555-556. [3] Herrick R.R. and Sharpton V.L. Lunar and Planetary Sci. Conf. 30, Abstract 1696. [4] Plaut J.P. (1993) Guide to Magellan Image Interp. 19-31. [5] Grimm R.F. and Hess P.C. (1997) Venus II 1205-1244. [6] McGovern P.J. and Solomon S. (1997) JGR 102,16303-16318. [7] Grimm R.E. and Phillips R.J. (1992) JGR, 97, 16035-16054 [8] Stofan E.R. et al. (1997) Venus II, 931-965. [9] Squyres S. W. et al. (1992) JGR 97, 13611-13634. [10] McGovern P.J. and Solomon S.C. (1998) JGR, 103, 11071-11101.

Table 2-Depressed Central Regions

Name	Width of Depression (km)	Max. Depth of Depressed Area (km)	Width of Base of Volcanic Edifice (km)	Height of Edifice (km)	Presence of Rim Embaying Flows
Kokyanwuti Mons	125	.7	50	.5	X
Itanua Corona	125	.75	66	.5	X
Uti Hiata	125	.4	NA	NA	
Nzambi Corona	137.5	.4	75	.4	X
Kunhild	175	.7	50	.8	X
Mielikki Mons	137.5	.5	60	.25	X

Techniques to Evaluate Microbial Contamination

Colin Griffin, Liverpool University, Liverpool, UK

Advisers : Carlton Allen and Eileen Stansberry (Lockheed-Martin, NASA)

Introduction

Recently work undertaken on the terrestrial contamination of meteorites has shown that microbes are present and actively growing inside these extraterrestrial materials [1],[2],[3],[4]. One of the urgent tasks at hand is to further classify this contamination to attempt to localise the source of contamination. Identification of the bacterial and fungal species may show whether the organisms are common microbiota associated with dust, human handling or are from a more environmental source ie. soil. The purpose of this current investigation was to compare an environmental soil sample against contamination from the Allende meteorite. To achieve this a standard culturing technique was chosen as well as the use of a more molecular approach ie 16srRNA identification.

Method

JSC-1 soil simulant (martian simulant) previously cultured by A. Steele was used as the environmental sample. The isolates were taken from stored culture plates and represent a subset of the possible organisms that were originally cultured by A. Steele. These organisms had previously been aerobically cultured on a range of media [5]. The frozen isolates were plated out onto Tryptic Soy Agar (TSA) in the form of a streak plate to enable easier isolation of single colonies. All plate manipulations (streaking, isolate harvesting, visual work and Gram stain [6] slide preparation were carried out in a lamina flow cabinet with appropriate aseptic technique). If during visual identification of the plate, there appeared to be only type of bacterial growth (a pure culture), a Gram stain was undertaken. The Gram stain results were observed under light microscope (Olympus BX-40).

After Gram staining identification of the cultures from pure culture plates was undertaken using the bioMerieux VITEK system, an industry standard automated bacterial identification system. This system achieves identifications using a small amount of bacterial in solution with sterile water, which is inoculated onto a test card that is chosen on the basis of the isolate's Gram stain result. Identification of the fungal isolates had already been performed based on their morphology, determined visually and by light microscope (Nikon HFXII).

In the characterisation of the microbial life on Allende, the process began with the preparation of a sample from the meteorite fragment. The sample comes from an unknown background, the

experiments were carried out on the sample as received from D.S. McKay. The sample had been stored in a plastic container. The preparation was performed by wrapping the meteorite in alcohol sterilised aluminium foil and fracturing the sample with a hammer. The foil package was transferred to lamina flow cabinet before further manipulations were performed. Chips were taken and some were ground into powder in a sterilised pestle and mortar. The powdered sample was stored in a sterile tube until needed. Larger chips were also retained for scanning electron microscope analysis. The organisms in the sample were cultured by two methods – on plates and in broth. The broth tubes were made up by adding 150mg of roughly broken chips to the media (Lethen broth) and treating them in an ultrasonic bath (Branson 1200) to disturb the cells from the rock surface. This was done by treating the sample for 20 seconds in the ultrasonic bath, then removing and agitating by hand. This was repeated three times. The tube was incubated at 35°C for 4 weeks before being streaked out on 5 media (TSA (a standard bacterial media), R2A (a minimal media), Sabraud dextrose media (SDX- a fungal growth media), an *Actinomyces* isolation media and MacConkey media (to support any Gram negative bacteria)). These plates were examined every 24 hours to remove isolates and replate them on the same media, as they appeared. This would prevent any plates becoming overgrown and make contamination easier to detect.

The powdered sample (100mg) was added to 3ml of sterile water and vortexed for 5 seconds before using the same ultrasonic treatment as outlined above. This suspension was then plated out on same 5 media outlined above. An anaerobic culture was also undertaken using boiled thioglycolate broth stored under Nitrogen. All plates and media were incubated at 35°C.

Once the isolates were taken from the plates, they underwent the same identification procedure as outlined on the JSC-1 isolates.

Results

-JSC-1 Martian soil simulant

The bacterial subset contained 43 isolates. 18 of these have no complete identification due mainly to a number of *Corynebacterium spp.* that were present and could not be further differentiated into individual species, as the VITEK system does not give accurate identifications of these, and they are to be characterised using molecular techniques. However, at the time of writing this abstract, this investigation is ongoing. The microbiota that could be classified

produced the following organisms : *Bacillus thuringiensis* (*B. thuringiensis*), *B. subtilis*, *B. pulvis*, *B. sphaericus*, *B. megaterium*, *B. cereus*, *B. licheniformis*, and *B. alvei*. Also present were the *Corynebacterium* and an *Actinomycete*, *Streptomyces*. There was also one other *Actinomycete* identified and further investigations are continuing on this isolate. The fungal species present in the sample were identified as follows : *Penicillium*, *Fusarium*, a *Hyphomycete* and *Aspergillus flavus*.

-Allende meteorite

The majority of the organisms in the Allende sample were Gram positive cocci. The prevalent species were *Staphylococcus auricularis* and *S. capitis*. Visual and microscopic morphology also identified *Micrococcus* species and some *Streptococcus* species.

The only non-coccioid organisms that were present were those cultured under anaerobic conditions. These results are pending and not available at the time of writing this abstract.

Discussion

The organisms found in the JSC-1 sample are all characteristic environmental species. The *Corynebacterium* and *Bacillus* are some of the most commonly found bacteria in the environment but are also common skin contaminants [7], [8]. The *Corynebacterium* need to be further analysed, for identification as do the *Actinomycetes*. This is underway using a more molecular based approach (16SrRNA), as opposed to the biochemical approach of the VITEK, as these species, especially the *Actinomycetes* are difficult to identify with a reliable amount of certainty. The advantages of using molecular techniques is the degree of certainty attained, a 150 base pair identification is sufficient for most organisms, but the entire 16SrRNA code of the organism can be determined and compared to databases. Phylogenetic trees can then be constructed to show how closely related by it's genetic material an organism is to other species. Fungi however cannot be identified by this technique currently (using the current facilities) and must still usually be identified on morphology alone.

Of the results gained, most came with a 99% certainty of correct identification. Those with lower certainties may be due to slightly mixed cultures on the plates, or contamination of the VITEK cards during preparation. The diversity and amount of species in the soil simulant show that currently, the JSC-1 simulant is not ideal as a standard. In handling experiments it would be exceptionally difficult to detect the appearance of one or two types of contamination, due to the density of life already

present. It also must not be over looked that these results represent only a fraction of the organisms in the simulant. The bacteria and fungi only show the organisms from around 25% of the original plates, due to contamination of the initial cultures. These samples were used as the isolates were removed and stored correctly before any contamination occurred. However, the original cultured subset would only identify those bacteria/fungi that are aerobic and copiotrophic (ie require high levels of nutrients) and the likelihood is that the majority of species in this simulant have not been detected in any way.

For use in sample sterilisation experiments, the JSC-1 sample shows more potential, as a distinct subset of organisms growing in defined cultures can be characterised. However, during these experiments the lack of a full characterisation of the cultured isolates limits this usefulness. In order for the soil simulant to be a reliable standard for microbiological tests, the experiment would need to be repeated. In the repeat, the following changes would need to be made to increase the potential for this to become a standard:

-After initial plate inoculation, the plates would need to be observed every 24 hours, to remove isolates as they appeared. The isolates should be streaked out, and part of the culture stored, so they could be used at a later date in case of contamination. A greater range of media, and especially an anaerobic environment would be useful to provide a greater subset of growth conditions, to enable a greater chance of gaining a true perspective of the microbial content of the simulant. However, this probably could only be achieved by the use of a more molecular approach. This would enable a more definite identification process, and a far greater number of organisms to be characterised. The preparation of simulant could be improved, so that it is at least covered from the air after it's collection, to prevent bacteria from the surroundings becoming a factor in it's microbial content. Wearing gloves whilst preparing the JSC-1 would prevent any skin-borne bacteria contaminating it especially the *Corynebacteria* whose presence in these cultures is probably due to handling. These two factors alone make the simulant a poor candidate for a standard as they can vary from sample to sample, leading to experiments having reduced reliability.

The Allende results point to only one source of the organisms present, terrestrial contamination. The *Staphylococcus* species is very commonly found both in soil, and on skin. The impact of this meteorite as well as any subsequent handling of the meteorite, and it's storage, would both have contributed to this. The poor diversity of organisms, in that only *S. auricularis* and *S. capitis* seem to be well established in the sample may be explained by the nature of these

organisms, as they are notoriously quick growing species, that may have become quickly established and prevented other species doing likewise [8], [9]. Their low tolerance for anaerobic conditions would explain their absence from the anaerobic plates and broth. The results from these plates are only at the Gram stain stage currently, but show little presence of cocci species. As few are present, the slower growing organisms may have more chance to establish themselves. This representation of growth throughout this sample of Allende can be compared in the future to the work currently being performed on Allende interior chips

Due to the sample's unknown recent history, it is most probable that the level of growth on it is greater than would be found on a sample that had been properly curated and handled. This is suggested in particular by the large amount of skin-borne bacteria present. The high level of growth that is seen in the Allende sample serves to show how easily contamination can occur, and how difficult it is to handle the sample in a manner to prevent this.

References

- [1] Steele.A et al, (1999), Abstracts of 30th LPSC. Imaging of unknown organisms on ALH84001 [2] Steele.A et al. (1999), Abstracts of 30th LPSC. Imaging of biological contamination of meteorites: a practical assessment. [3] Steele.A et al, (1999), Abstracts of 30th LPSC. Contamination of the Murchison meteorite. [4] Toporski.J.K.W et al, (1999), Abstracts of 30th LPSC. Contamination of Nakhla by terrestrial microorganisms [5] Allen.C et al (1999). Effects of sterilising doses of gamma radiation on Mars analog rocks and minerals [6] Difco Manual, 10th edition [7] Bergey's Manual of Systematic Bacteriology (1984). Volume 1. [8] Manual of Environmental Microbiology, Hurst.C.J et al. (1997) [9] Bergey's Manual of Systematic Bacteriology (1986). Volume 2.

Acknowledgments

Thanks to Carlton Allen and Eileen Stansberry for their time and patience, and to Andrew Steele for all the help. Thankyou also to Tatjana Modlina and Tom Molina for the previous work on JSC-1, and to Theron Groves, Duane Pierson and Mark Ott for all the advise and experience shared. For the guidance throughout, thanks to David McKay, Kathy Thomas-Keptra and Sue Wentworth.

The thermal structure of Venus: a flexural analysis

Emma-Kate Potter, Australian National University
Walter Kiefer, Lunar & Planetary Institute

Introduction: In order to explain Venus' thermal history, it is important to understand the thermal structure of the outer layers of the planet. Does Venus, in general, have a thick thermal lithosphere with a corresponding small thermal gradient and low heat flow or is this layer relatively thin with a higher heat flow similar to that of the Earth? Physical properties of Venus' lithosphere are related to its thermal structure. In particular, the thickness of the effective elastic layer is dependent on the thermal gradient. Previous attempts have been made to determine the depth of this elastic lithosphere using methods such as flexural analysis based on topography observations [1]; and admittance studies (topography-gravity) over larger scale regions [2-4]. However, many of these analyses have concentrated on regions now recognised as the surface manifestation of upwelling mantle plume structures. It has been pointed out that individual volcanic features on these large volcanic rises may be partially supported by a dynamic mechanism associated with the upwelling. Further, even though the dominant gravity variations associated with these regions are at longer wavelengths, it is also dynamically possible for the mantle plume to contribute smaller wavelength structure to the gravity field [2,5].

The aim of this study is to investigate the properties of the elastic lithosphere without the complicating factors of dynamic support. To achieve this, I have chosen a number of volcanoes in regions not directly associated with mantle upwelling. Assuming a basalt crust with a density of 2900 kg/m^3 and a thickness of 25 km [6], flexural calculations are performed for a model load for each volcano. The resulting deflection and free air gravity anomaly is then calculated for a given elastic thickness. This calculated gravity signal is filtered for comparison with the observed, lower resolution gravity data. This comparison leads to a determination of the most appropriate value of elastic thickness for that region. From the elastic thickness, we can estimate the lithospheric thermal gradient for the region.

The Model: There are more than 160 features classified as large volcanoes ($>100 \text{ km}$ diameter) on Venus [7,8]. However, only a small number are suitable for the analysis presented here. The most important criterion for selection is that the volcano is in an area of low geoid and minimal long wavelength geoid structure. Since mantle upwelling is generally associated with high geoid, this condition ensures that the only support mechanisms are flexure and isostasy. Due to the nature of the flexure-gravity calculation and the resolution of the Magellan gravity data, selection of volcanoes is also constrained by their having a radius of more than 100 km and a height of more than 1 km. Additional constraints vary between volcanoes and depend largely on the quality of the topography and gravity data, asymmetry of the volcano, and the proximity of surrounding features.

Following the flexure calculation of Melosh [9], each volcano is modeled as an axisymmetric gaussian load (see Kali Mons, Figure 1a). For a given elastic lithospheric thickness, the deflection of the lithosphere and the corresponding free air gravity can be determined. As elastic thickness increases, the low density root produced by the deflection of the crust will thin. As a result, the mass excess on top of the crust will not be as fully compensated by its low density root and the free air gravity anomaly will increase accordingly. Some volcanoes require more than one gaussian to appropriately model the load (see Kunapipi Mons, Figure 1c). Since the gravity calculation is linearly dependent on the load contributions, in these cases, the total free air gravity is simply an addition of the two (or more) components. The calculated gravity is based on a high-resolution topography (5 km). However, the free air gravity data from Magellan used for this analysis has a much lower resolution (up to 120 degree spherical harmonic, dependent on location [10]). For this reason, the calculated gravity must be filtered for comparison. This was done by truncating a Bessel function expansion of

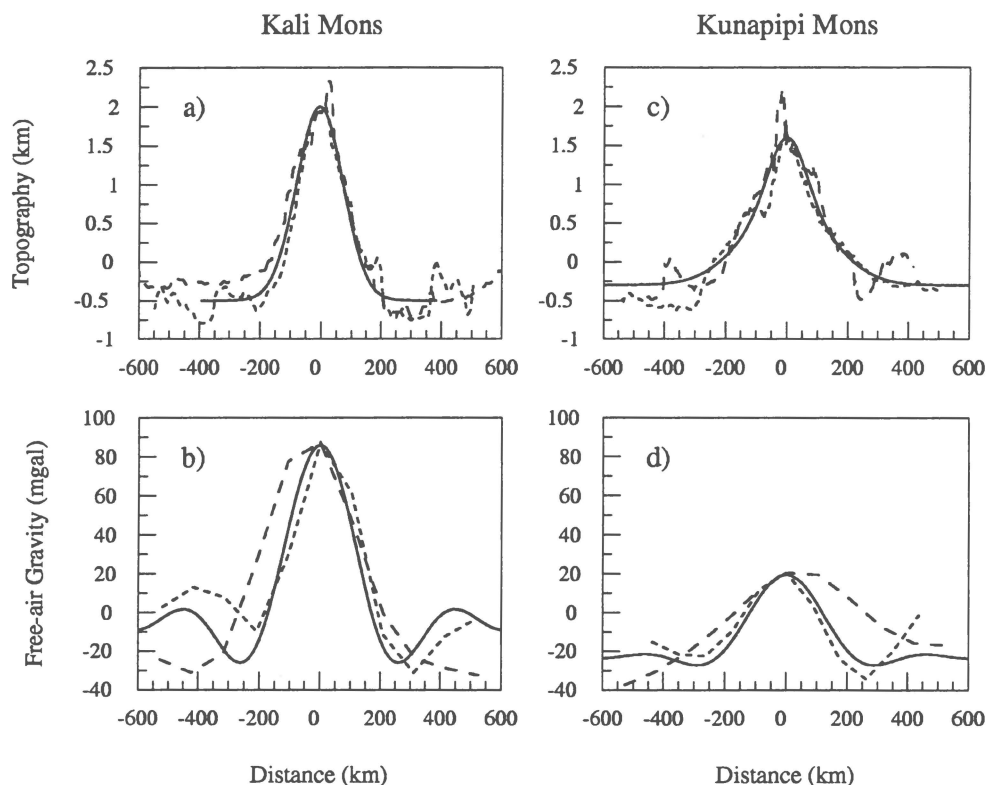


Figure 1: a) Kali Mons observed EW & SN topography profiles (dashed & dotted) with topography model (solid). b) Kali Mons observed free air gravity profiles (dashed and dotted) and calculated free air gravity (solid) for 20km elastic thickness. c) Kunapipi Mons observed and modeled topography d) Kunapipi Mons observed free air gravity and calculated for 10km elastic thickness.

the calculated gravity to an appropriate value, dependent on the location of the volcano on the planet.

It is important to note that it is not necessary for the topography model to include all observed small wavelength variations since the gravity filtering process removes any of the small wavelength gravity variations (Figure 1a,c). There are some uncertainties introduced to the elastic thickness determination as a result of the choice of filter. The most appropriate filter is chosen based on the degree strength of the Magellan data for that particular location and a range of uncertainty for elastic thickness is then estimated by using different filters on either side of the best fit.

Uncertainties are associated with the observed gravity field and these are generally the major component of the error stated for the elastic thickness calculations discussed below. To determine these uncertainties, the elastic thickness is determined for a gravity profile with

a magnitude of its given value plus or minus twice the stated gravity data uncertainty. In practice, the mapped uncertainties in the gravity field are roughly a factor of 2 too large at the short wavelengths of interest to this study [10] so our error estimates are quite conservative.

Results and Interpretation: A summary of the volcanoes studied and the elastic thicknesses determined are given in Table 1. The volcanoes appear to fall in two distinct groups: those with mean elastic thickness around 10 km or less and those around 20 km. Both sets of elastic thickness estimates are at the lower end of the range previously stated for Venus' elastic lithosphere [1-4].

Sekmet Mons and Atira Mons, in the northern plains, are far removed from any hot-spot activity and the elastic thickness for each is calculated to have an upper limit of about 10 km. Similarly, Kunapipi Mons (Figure 1c,d) is located

Volcano	Region	Lat/Long	T _E (best fit)	T _E range
Kali Mons	E. Eistla	9N 29E	20km	15-30km
Emma-Kate Mons*	E. Eistla	3N 45E	22km	15-35km
Hathor Mons	Dione	40S 325E	22km	11-30km
Innini Mons	Dione	34S 329E	17km	10-30km
Sekmet Mons	N.Plains	44N 241E	≈0km	<10km
Atira Mons	N.Plains	52N 267E	<10km	<10km
Tuuliki Mons	S. Beta	10N 275E	8km	3-15km
Kunapipi Mons	S. Plains	34S 86E	10km	0-18km

*Table 1: Summary of Volcanoes analysed and calculated elastic thicknesses (T_E)
(*name not yet approved by IAU)*

in the southern plains, with a very low geoid and its elastic thickness is calculated to be around 10 km. Tuuliki Mons is located between the apparent hot spot regions Beta and Phoebe Regiones but its geoid is low and its elastic thickness calculated to be around 8 km.

In contrast, there are two sets of volcanoes located in regions with slightly higher geoid and in closer proximity to possible hot spot regions. Hathor Mons and Innini Mons of Dione Regio and Kali Mons (Figures 1a,b) and Emma-Kate Mons (name yet to be approved by IAU) near Eastern Eistla all give values of about 20 km. The range of uncertainty in the elastic thickness calculation for each volcano is given in Table 1. These uncertainties are based on both the filter choice and the stated error in the Magellan gravity data. There are three distinct pairs of data points that are closely spatially related. In each case the two estimates of elastic thickness agree well within the uncertainty range, further confirming the assertion that the uncertainty ranges presented in Table 1 are conservative.

In general, previous calculations of elastic thickness lie in the range 20 to 40 km and are therefore notably higher than the results presented here. This supports the hypothesis that earlier results were influenced by underlying mantle dynamics and indicates that the elastic lithosphere as a whole may be thinner than previously thought.

The interpretation of the elastic thickness calculations in terms of thermal structure of the Venus' outer layers is based on assumptions about the behavior of the materials that make up the crust and upper mantle. A first order determination of the thermal gradients is made

here. The upper crust is dominated by a brittle, sliding regime where strength increases with depth. At some depth, the temperature is such that viscous flow dominates and, consequently, the material's strength will decrease with depth. This transition between brittle and viscous behavior forms a 'strength envelope' that is strongly dependent on the temperature gradient. The base of the elastic lithosphere is defined as the point at which the strength of the material is less than 50 Mpa [11].

For those elastic thicknesses calculated to be around 10 km or less, the corresponding thermal gradient is larger than 15 K/km. This corresponds to a heat flux out of the mantle of at least 60 mW/m² that is similar to the observed average mantle heat flux on Earth. The regions with larger elastic thicknesses will have lower thermal gradients. More precise estimates for the thermal gradient using McNutt's [12] mechanical lithosphere calculation will be derived in a later phase of this study.

[1] Johnson and Sandwell (1994), *Geophys. J. Int.*, **119**, 627-647; [2] Smrekar *et al.* (1997) *Venus II*, Univ. Arizona Press, 845-878; [3] Phillips *et al.* (1997), *Venus II*, Univ. Arizona Press, 1163-1204; [4] Simons *et al.* (1997), *Geophys. J. Int.*, **131**, 24-44; [5] Kiefer (1998) LPSC 29 abstract 1887; [6] Grimm and Hess (1997), *Venus II*, Univ. Arizona Press, 1205-1244; [7] Crumpler *et al.* (1997), *Venus II*, Univ. Arizona Press, 845-878; [8] McGovern and Solomon (1998), *JGR*, **103**, 11,071-11,101; [9] Melosh (1978), *Proc. Lunar Planet. Sci. Conf.* 9th, 3513-3525; [10] Konopliv *et al.* (1999), *Icarus*, **139**, 3-18; [11] Bodine *et al.* (1981), *JGR*, **86**, 3695-3707; [12] McNutt (1984), *JGR*, **89**, 11,180-11,194.

Piercing the Clouds: Stratigraphy of Mare Nubium

Danielle E. Rose, Southern Oregon University, Ashland, OR

Advisor: Paul D. Spudis, Lunar and Planetary Institute, Houston, TX

INTRODUCTION

The Moon has two distinct geologic provinces, as dissimilar and recognizable as the continents and oceans of Earth. The pockmarked highlands make up the greater portion of the near side, but the eye is drawn to the darker, smoother maria. The maria cover 30% of the near side, but only represent 16% of the moon's surface. Even before samples were returned to Earth, geologists had correctly concluded that the smooth, flat surfaces of the maria were the result of fluid, lavalike emplacement, much like terrestrial basaltic lavas [1].

Although the maria seem uniform, previous work has shown that they were created during a prolonged episode of basaltic volcanism [4]. Determining the sequence, duration, and composition of basalt flows in the maria allow us to reconstruct the volcanic history of the Moon. Such studies are important for understanding lunar thermal history and planetary bulk composition.

Mare Nubium, the focus of this study, is located in the south-central region of the near side. An area from 0-30 degrees S and 0-30 degrees W was examined using the multispectral data obtained by the Clementine mission in 1994. These images enabled us to map compositionally different lava flows within the mare. Some post-mare craters have thrown out ejecta of distinct composition that differs from the surrounding lava. Such craters were examined in order to derive, through a simple technique, the thickness of the mare at that particular point. These points were then used to construct a mare thickness map of the Nubium basin. In addition to this, Lunar Orbiter IV photos were used to determine the crater density of each flow, to estimate the relative ages of each flow. Absolute ages are predicted by comparing these densities to those of mare flows sampled and dated by Apollo.

METHODS

Clementine orbited the Moon in a polar orbit, taking data in longitudinal swaths. These swaths are assembled into a mosaic of regional composites; one mosaic may be comprised of several orbits. The raw data is processed using ISIS software from the USGS [10], where it is photometrically corrected, reprojected, and joined together seamlessly into the large mosaic. The mosaic is composed of three spectral bands, taken at the 950, 750 and 415 nm wavelengths. Each band is assigned a color: red, green and blue, respectively. The combination of the three produce a quasi-"true color" image of Mare Nubium, in which the color is subtly

enhanced in comparison to the naked-eye view of the moon. Highlands appear slightly reddish, and maria tend more towards the blue end of the spectrum. If the values in these separate bands are ratioed, however, with 750/415, 750/950 and 415/750 representing red, green and blue, and combined once more, a dramatically colorful and highly valuable "false-color" mosaic emerges. This false-color composite is an extreme stretch of the true-color mosaic, where highlands appear bright red, and lavas, although spanning a range of colors, tend towards blues and purples.

In addition to the true-color and false-color mosaics, I used the mapping techniques of the Hawaiian group [2,3] to make images of the iron and titanium concentrations over the area. This processing removes the effects of maturation that interfere with the compositional dependence of spectral reflectance, and, in conjunction with data from sampled sites on the Moon, permits iron and titanium mapping of regional areas at full Clementine resolution (200 m/pixel). This mapping technique has been validated by newly obtained Lunar Prospector iron and titanium gamma-ray data [11]. These maps play a key role in determining the composition and thickness of the mare lavas.

PROCEDURE

I first mapped compositionally different flows, using a combination of the false-color mosaic, and the iron and titanium maps (Figure 1). Because the Apollo samples were remarkable for their relatively high titanium content and variation [8], and because titanium can be determined by spectral reflectance [3], mare basalts are arbitrarily broken down into categories by titanium content: high-Ti (>9 wt. % TiO_2), low-Ti (1.5-9 wt. % TiO_2) and very-low-Ti (<1.5 wt. % TiO_2). All of the flows in Mare Nubium fall into the low-Ti category, and I further subdivided them into "low" and "medium" titanium flows.

Once mapped, I studied each flow in detail, to determine their iron and titanium contents. After careful mapping, I can identify five compositionally distinct units (Table 1). The flows were mapped in as much detail as possible; however, in some areas the mare surface was obscured by prominent ejecta and rays from large, post-mare craters, and this made the mapping process difficult.

Once the geologic map was refined, and the mare lava flows classified by composition, I measured crater densities (number of craters per km^2) on Lunar Orbiter IV photos for each flow. Cumulative numbers of craters larger than 500 m were counted in a defined area of each flow, and larger flows were sampled in several locations to assure an accurate representation of the flow. These crater densities were compared to the densities at Apollo sites, where we have dated samples from which to estimate their absolute ages. On the basis of estimates from these dated Apollo samples, the Nubium flows range in age from 3.0-3.7 Ga.

To determine the lava thickness, each flow was examined for craters between one and ten km in diameter, which have ejecta visibly lower in iron than the surrounding mare lava. This indicates that the crater has "punched through" the lava and into the anorthositic highland material below [8]. For the smaller flows, only a handful of craters fit both the size and compositional criteria, but the more expansive flows had 50 or more craters to provide data points. For the purpose of quick estimates, I used a simple cylindrical model of the crater excavation cavity in which the depth of excavation equals 1/10 the observed diameter, values in accordance with those determined from cratering studies [9]. The fraction of high-iron maria seen in each crater ejecta blanket is converted to an equivalent thickness of lava at each crater target site. Each lava flow used an individual model, tailored to the observed iron content of the highlands material nearby, and the overall iron content of the flow. Once thicknesses were determined, points were contoured into an isopach map (superimposed on a simplified map of the region), to show mare thickness variation and to represent the topography of the underlying Nubium basin floor (Figure 2).

From the isopach map, I extracted the volume of mare lava by finding the area (or combination of multiple areas, in this case) enclosed by each isopach, and multiplying that area by the 0.1 km interval to produce the volume in cubic kilometers. This procedure also took into account, and subtracted out, the scattered islands of highland material within the basin. Once the volume of each interval was tabulated, the overall volume of the mare was calculated: Mare Nubium consists of approximately $111,000 \text{ km}^3$ of lava. For the entire region of study, the volume of crust present (based on an average 60 km crustal thickness) was calculated to be $47,673,000 \text{ km}^3$. Thus, although Mare Nubium covers 45% of the area studied, it represents only 0.2% of volume of the crust in the area. This fraction is consistent with studies of other maria [4].

STRATIGRAPHIC HISTORY OF NUBIUM

The oldest unit of the Nubium region is the highlands crust and the materials that make up the basin

itself. An eruption of low-Ti basalt (L_1) occurred at 3.7 Ga (Table 1), covering a minimum area of $41,000 \text{ km}^2$, and averaging 260 m in thickness. This unit may underlie subsequent flows, but I have not been able to determine its subsurface extent, if any. This was followed by three eruptions of mid-Ti lava at 3.5 Ga. Unit M_1 covers an area of $10,000 \text{ km}^2$, averaging 380 m in thickness. This unit occurs in two separate patches, on the far western side of the region. Flow M_2 has an average of 230 m thick over a $20,000 \text{ km}^2$ area, and is the brightest flow on the titanium map. Unit M_3 has an area of $12,500 \text{ km}^2$ with an average thickness of 480 m, and is almost as titanium-rich as M_2 . It is possible that the two are actually the same unit, since they are almost identical in both age and composition. The next eruption (L_2) occurred at 3.4 Ga, extruding a low-Ti lava and covering a small patch, $2,000 \text{ km}^2$ in area, with an average thickness of 415 m. L_2 has an identical composition to the first unit, L_1 , but is considerably younger. The last event occurred at 3.0 Ga, erupting a medium-Ti lava (M_4), covering a area of $275,000 \text{ km}^2$ with an average thickness of 380 m.

The various lava eruptions of the Nubium region lasted about 700 Ma. Given the eruption duration and volume, this part of the Moon had a magma production rate of $1.6 \times 10^{-4} \text{ km}^3/\text{a}$. The production rate of the rest of the near side during the late Imbrian is $150 \times 10^{-4} \text{ km}^3/\text{a}$, as reported by Head et al; either Mare Nubium was unexpectedly quiescent during this period of time, or the estimated rates [4] are anomalously high. For comparison, current terrestrial rates for Mount Vesuvius is $1.07 \times 10^{-2} \text{ km}^3/\text{a}$, and for Kilauea is $1.7 \times 10^{-2} \text{ km}^3/\text{a}$ [4].

CONCLUSIONS

Mare Nubium has undergone a prolonged and complex volcanic evolution. Multiple flows of different age and composition have resurfaced the basin floor, and although the flows in Nubium are prominent, they are actually quite thin, in accordance with a variety of previous studies [5,6,7]. On the basis of the age and volume estimates presented here, I deduce that the Moon, while volcanically "active" more than 3 billion years ago, was orders of magnitude below the levels of geological "activity" observed on Earth. Vast periods separate each mare flow in Nubium and the picture of lunar volcanism derived from this work suggests rapid, effusive eruptions of high volume flows, possibly lasting only a few weeks or months, followed by extended periods of dormancy. The techniques and approaches followed here can be profitably applied to other lunar maria, allowing us to decipher the complex story of lunar volcanic history on a global basis.

REFERENCES:

[1] Wilhelms, D., 1987, USGS Prof. Paper 1348, p. 85, [2] Lucey, et al, 1995, Science, v. 268, pp. 1150-1153, [3] Blewett, et al, 1997, JGR, v. 102, pp. 16319-16325, [4] Head J.W. and Wilson L., 1992, Geochim. Cosmochim. Acta 56, 2155-2175, [5] De Hon, R., 1979, PLPSC 10, 2935-2955, [6] Horz, 1978, PLPSC 9, 3311-3331,

[7] Rhodes, J.M., 1977, Philos. Trans. Royal Soc. London A285, 293-301, [8] Heiken, G., et al (eds.), 1991, Lunar Sourcebook, chap. 6, [9] Heiken, G., et al (eds.), 1991, Lunar Sourcebook, chap. 4, [10] ISIS documentation homepage at <http://wwwflag.wr.usgs.gov/isis-bin/isis.cgi>, [11] Elphic R.C., et al, 1998, Science 281, 1493-1496.

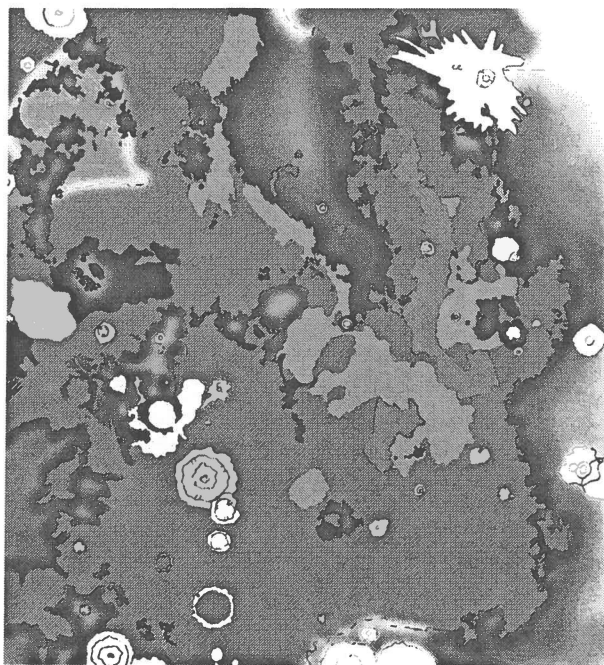


FIGURE 1 – Geologic map of Nubium region. As a guide, browns are highlands, outlined or white areas are craters and ejecta. L_1 and L_2 flows are orange, M_1 is light yellow, M_2 is blue, M_3 is deep red and M_4 is the purple that covers most of the region. For scale, 1 cm : 24 km.

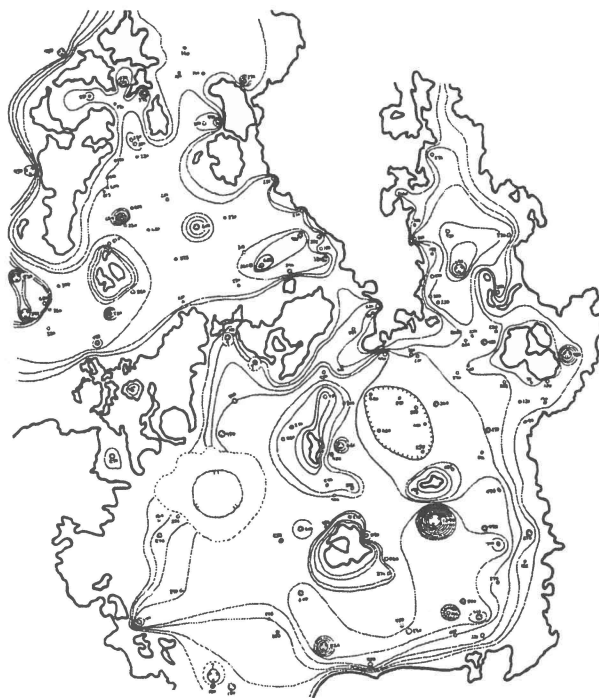


FIGURE 2 – Isopach map of Nubium region. All depths expressed in m, isopachs are in 100 m increments, areas with tickmarks along the inside of the isopach are areas of local shallowing within the mare. Simplified highland boundaries appear as thick lines. Dashed boundary encloses area obscured by ejecta. For scale, 1 cm : 24 km.

TABLE 1: Mare Nubium Flow Data

UNIT	CRATER DENSITY	AGE*	COMPOSITION		THICKNESS (m)			EXPOSED AREA
	$N/km^2 (10^{-2})$		FeO	TiO ₂	Min.	Max.	Avg.	km^2
L_1	$7.6 \pm .28$	3.7	22%	3.5%	70	460	260	41,000
M_1	$6.6 \pm .26$	3.5	22%	5%	200	630	380	10,000
M_2	$6.5 \pm .25$	3.5	23%	6.5%	130	295	230	20,000
M_3	$6.4 \pm .25$	3.5	23%	6%	360	840	480	12,500
L_2	$5.4 \pm .23$	3.4	22%	3%	400	430	415	2,000
M_4	$3.8 \pm .19$	3.0	22%	5%	70	1340	380	275,000

* Ages interpolated from known Apollo sample dates: Apollo 11, 3.7 Ga with a crater density (N/km^2) of 8.0×10^{-2} ; Apollo 15, 3.3 Ga with a crater density of 5.0×10^{-2} ; Apollo 12, 3.1 Ga with a crater density of 4.5×10^{-2} .

“Mapping the Impact Crater Asymmetry on Ganymede”

Steven Sobieszczyk
University of Wisconsin, Oshkosh, WI

Advisor: Dr. Paul Schenk
Lunar and Planetary Institute, Houston, TX

Introduction

Ganymede (Figure 1) is the largest satellite in our solar system. Along with Io, Europa, and Callisto, it is one of the four Jovian moons. Abundant resurfacing and recent evidence for a magnetic field indicate a dynamic geologic history for ice-rich Ganymede. Two types of terrain are evident on its surface: a dark, older terrain with an extensive cratering history, and a bright, grooved and smooth terrain, which is relatively younger. Previous estimates date the dark terrain as being over 4 Ga [1] while estimates for the bright terrain range from 0.5 to 1 Ga [5] up to 3.8 Ga [2]. Roughly 2/3rds of the satellite has been resurfaced by this bright terrain.

Despite resurfacing, all of Ganymede has experienced some cratering. Heavy bombardment has left the surface scarred with at least 1000 craters with diameters greater than 20km. Several different types of comets and asteroids may be responsible for this cratering on Ganymede, including: Jupiter Family Comets (JFC), Long Period Comets (LPC), Halley-type comets (HTC), trojan asteroids and planetocentric debris. JFCs are short period comets (orbital periods <20yr) that are influenced by Jupiter's gravity. LPCs and HTCs (orbital periods >20yr), are typically grouped together, and are the other type of comet. Modeling by Zahnle et al. [3,4] suggests that JFCs make up around 90% of the impacts and LPC/HTCs make up about 1-10% [3,4]. Planetocentric debris orbiting Jupiter and trojan asteroids

(objects co-orbiting with Jupiter in the L4 and L5 stable resonances) [4] may make up <10% of Ganymede's crater population.

The cratering rate on Ganymede is predicted to be asymmetric [3,4] due to synchronous rotation. If a satellite is locked in synchronous rotation with a planet, one hemisphere always faces forward. The central point on the leading hemisphere is termed the *apex*, and converse is the *antapex*. The leading hemisphere, theoretically, will be substantially more cratered than the trailing hemisphere [3,4]. It is like throwing a knuckleball (non-rotating) through a swarm of bees. More bees will hit the front than the back of the ball. In the case of Ganymede, the asymmetry varies depending on whether JFCs, LPC/HTCs, and/or asteroids are dominant [4].

Data Analysis

Voyager obtained the first images of Ganymede in the late 1970's. Unfortunately, the areas between 45-105° and between 240-300° were not imaged at high resolution. These areas include the apex and antapex, respectively. With this data missing, early investigations [3] suggested a lack of asymmetry for Ganymede. We have used new data from Galileo (E6 and G9 orbits) to map the crater distribution in the apex and antapex regions, and search for a crater asymmetry on Ganymede.

We divided the apex and antapex regions into 20° concentric rings extending

out to 50°. We then further focused our area of study by mapping craters only on bright terrain. This was important because the possibility that the same event that brought Ganymede into its current orbital resonance may have created the energy necessary for Ganymede's resurfacing (namely the formation of bright terrain) [5]. Speculation has also suggested that Ganymede may have rotated non-synchronously for an unknown period of time, possibly in association with capture into orbital resonance [4,5]. By focusing on the crater density of the bright terrain, we may be able to estimate the age of the terrain and/or the time period when it rotated non-synchronously.

All craters down to 30km in diameter were measured and mapped in our study area. The crater count divided by the area determined the crater density. Table 1 shows our results. A least-squares fit through our data (Figure 2) indicates that the overall crater density ratio between the apex and antapex is 4:1.

Discussion

Calculations by Zahnle et al. [4] predict a crater density ratio at least 24:1. Our observed 4:1 asymmetry is at least six times less than that predicted by Zahnle et al. for JFCs (Figure 2). There are two possible explanations for the difference between the predicted and measured asymmetry. First, the previous assumption that Ganymede has always been locked in synchronous rotation is incorrect. Possibly, during the formation of the current tidal resonance, Ganymede experienced uniform cratering as it rapidly rotated. Later, when its orbital period matched that of today, a crater asymmetry began to form on bright terrain. This multiple stage history would dilute Ganymede's crater density asymmetry. Our data suggests that uniform

cratering during 45% of the post bright terrain history would be required to explain the observed crater population.

The second possible explanation focuses on the assumptions regarding impact source material. Zahnle et al. estimated that 90% of the crater forming projectiles are JFCs. The abundance of LPCs or planetocentric debris, after the time of bright terrain formation, may have been greater than was originally thought. If the percentage of JFCs were lowered to 50-60%, the observed crater asymmetry could also be explained.

References

- [1] Pappalardo, Robert T. *The New Solar System*, pp.263-275.
- [2] Shoemaker, E.M. et al. (1982) *Satellites of Jupiter*, pp.435-520
- [3] Shoemaker, E.M and R.F Wolfe. *Satellites of Jupiter*, pp277-339.
- [4] Zahnle, Kevin. (1998) *Icarus 136*, pp. 202-222
- [5] Malhatra, R. (1991) *Icarus 94*, pp. 399-412.

Crater Density for Bright Terrain

Distance to Apex	N>30km	N>10km
0-20°	14.69	164.71
10-30°	15.90	178.26
20-40°	16.10	180.52
30-50°	13.82	155.00
150-130°	5.14	57.58
160-140°	4.48	50.24
170-150°	4.08	45.70
180-160°	3.09	34.64

Table 1. Crater Density on Ganymede. Using known data for craters with diameters >30km, we calculated the equivalent at >10km. This was done with the power law $N(>D)=cD^{-2.2}$. Where N= the crater number, D= crater size, and c=constant. Plotted on Figure 1.

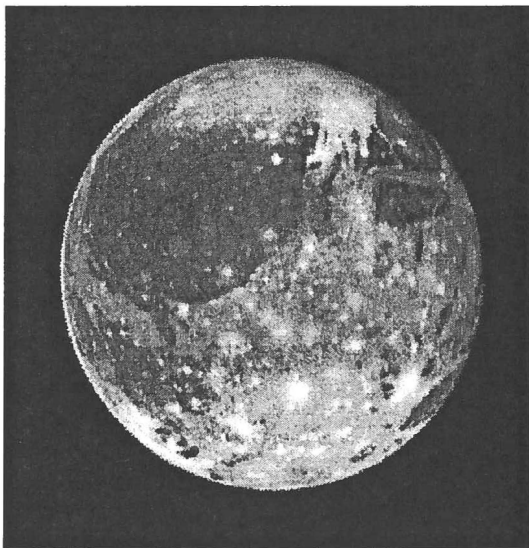


Figure 1. Ganymede

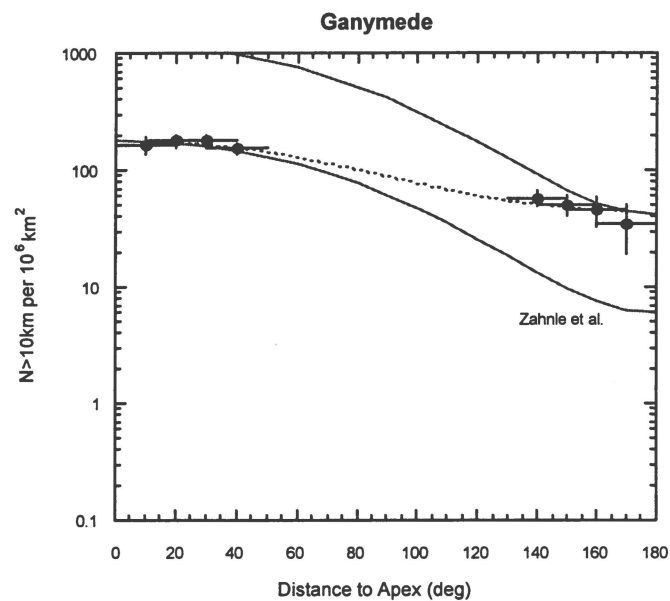


Figure 2. Crater Density as a function of distance from apex. Dark curves are predicted crater densities for JFCs [4]. Dotted line is least-squares fit to our data (filled circles).

The Modal Composition of the Kaibab Formation at Meteor Crater, AZ

Lora Varley, North Carolina State University, Raleigh, NC
Friedrich Hörz, NASA Johnson Space Center, Houston, TX

Introduction:

Impact melts tend to be remarkably homogeneous compositionally considering the diversity of rocks that may compose a crater's target [1,2,3]. This mandates exceptionally efficient mixing mechanisms. Details of this mixing process are poorly understood at present, largely because most terrestrial craters are deeply eroded, rendering reconstruction of the detailed pre-impact stratigraphy impossible in most cases. As a consequence, it is not well known even for well-studied terrestrial craters from what stratigraphic depth the dominant volumes of impact melt derive. Clarification of this question has significant applications for the source depth of planetary impact melts, especially those from the Moon, some of which are known to derive from specific craters or basins. Knowledge of a melt's source depth in the context of basin forming impact would allow substantial inferences about the compositional and lithologic make up of the lunar crust.

To hopefully improve our current understanding from which target depth(s) most melts derive, a group at JSC [4] is currently analyzing the melts from Meteor Crater (MC), AZ. This 1 km diameter crater ranks among the best investigated impact structures on Earth and its target is well characterized [5,6]. It is composed of sandstone (Moenkopi and Coconino Formations) and dolomitic limestone (Kaibab Formation).

Somewhat unexpectedly, preliminary analyses at JSC show that the impact melts at Meteor Crater fall into two compositionally distinct groups that differ predominantly in Fe, but also in Ca and Mg. The Fe is substantially derived from the iron meteorite projectile, and variable Fe content simply implies variable contributions to the melt by the projectile. In contrast, the systematic differences in Ca and Mg must reflect target properties. Specifically they relate to the detailed mineralogical and compositional make up of the Kaibab Formation, a dolomitic limestone, some 80 m thick at Meteor Crater, supplying virtually all of the Ca and Mg in the melts. The detailed distribution of Ca and Mg in vertical profile becomes therefore of interest at MC and is the subject of this project. Approximately 60 samples were available that were collected every 1-2 m, in carefully documented vertical profile, from Kaibab exposures in the walls of MC.

Experimental Methods:

X-ray diffractometry (XRD) reveals the characteristic lattice spacing of specific minerals present in a powdered sample. Relative peak height of specific lattice planes reflects the relative abundance of individual minerals within any given mineral mixture. Absolute mineral concentrations require the use of standard powders, which contain the minerals of interest in known proportions to allow for empirical analysis of the unknown sample, principally by ratioing the amplitudes of the major diffraction peaks of specific minerals. The method is relatively fast and thus well suited for a large number of samples, yet its accuracy is limited and at the level of 10 % (weight).

A Scintag XDS 2000 diffractometer was used, including a copper ceramic tube at 45 kV and 40 mA tube current. Data were collected in step-scan mode in the angular range $20 - 60^\circ 2\theta$ with step width $0.03^\circ 2\theta$ counting continuously at $1 \text{ degree min}^{-1}$. Sample mass was approximately 1.43 g for all XRD runs. The standards were composed of pure, single crystal quartz and dolomite ground to grain sizes less than $63 \mu\text{m}$ and mixed in differing proportions. The Kaibab samples were similarly ground to grain sizes less than $63 \mu\text{m}$.

Results:

Figure 1 illustrates some representative XRD scans for standards as well as Kaibab materials. Fig.1d summarizes all data. Specifically, the relative intensities of the quartz and dolomite peaks were plotted against absolute quartz content, the remainder being dolomite in this 2-phase mixture. A linear regression was used to obtain a trendline for the standard samples; this line fit was then used to calculate the percentage of quartz in each Kaibab sample. Note the uncomfortable scatter of the standard powders; however, this is not atypical for XRD, the reason why it is only useful at the 10% level of modal abundance. In detail, this scatter may be caused by lineation effects of a powder that was compressed into a sample well; also, variable grain size (at scales $\ll 63 \mu\text{m}$) may play some role.

A truly surprising result was that none of the Kaibab samples revealed any substantial quantities of calcite, yet abundant quartz, via XRD (see Fig.1). Because the Kaibab is often referred to as "limestone", we expected the calcite to be omnipresent and indeed we initially had prepared

XRD standards that contained quartz, dolomite, and calcite. However, the paucity of calcite and abundance of quartz seems consistent with McKee's (1938) [7] general descriptions of Kaibab as a highly variable sequence of near-shore sediments containing abundant clastic quartz, sandy dolomite, Mg-rich limestone, pure limestone, sandy limestone, and even genuine sandstone, etc. These substantial facies changes over short distances, typical of near-shore environments, are evident at MC. The closest reference profile detailed by McKee (1938) is from the Walnut Canyon, some 40 km to the West of MC, which contains genuine sandstone and "limestone" as well.

Figure 2 summarizes all measurements in vertical profile and places them into stratigraphic context. Individual samples were taken within lithologic context in the field as determined by such criteria as massive versus bedded sections, soft (eroded) versus hard (cliff-forming) layers, or simply on the basis of color, ranging from rusty brown to tan. Massive strata, of darker color shades, form distinct cliffs at higher elevations (60-95 m). However, the most quartz rich samples are generally soft and easily eroded beds, typically < 1 m in thickness and of subordinate stratigraphic significance. The XRD results do not suggest any systematic, lithologic change in the presence of quartz with increasing depth in the Kaibab at MC. Individual subsections, at scales of 10 m, may show some cyclic behavior in the abundance of clastic quartz, most likely due to the transgression and regression of ancient shorelines. The high quartz content averages some 55 % for the entire Kaibab Formation, and the remainder is dolomite.

Conclusions:

The modal analysis of Kaibab samples via XRD identifies the major stratigraphic section at Meteor Crater, AZ to be composed of dolomite and quartz in highly variable proportions. These results complement and corroborate the limited number of chemical analyses of Kaibab samples, and especially of melts, available at JSC [3]. Both data sets reveal that the Kaibab Formation is lithologically heterogeneous on meter scales, yet it does not change compositionally in systematic fashion with stratigraphic depth. The compositional grouping of melts based on differences in their CaO and MgO content can therefore not be assigned to systematically different source depth(s) within the Kaibab. The differences are obviously due to the incomplete mixing of specific, yet arbitrary, subsections of Kaibab. On the other hand, the surprisingly high quartz content of Kaibab opens the possibility that

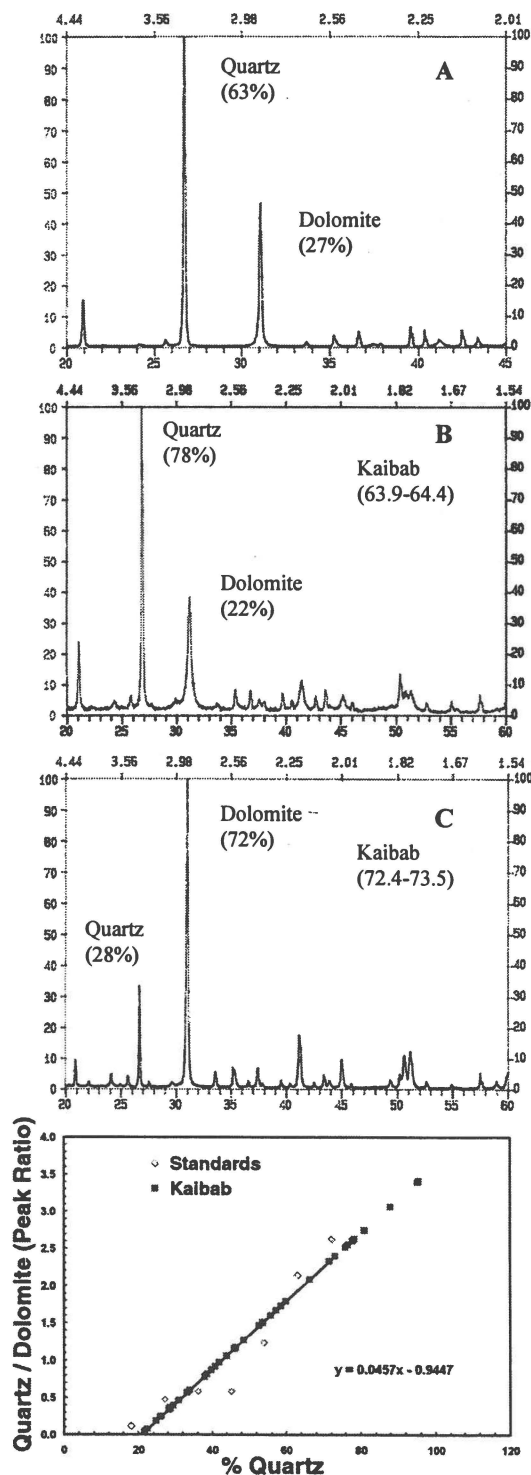


Figure 1. XRD plots for a standard (A) and two Kaibab samples (B, C) show differing peak intensities according to different mineral concentrations. The standard trendline was used to calculate the abundance of quartz in Kaibab samples (D).

the melts at Meteor Crater represent the CO₂ depleted, refractory residue of Kaibab, with minor contributions from the approximately 10 m thick Moenkopi sandstone above, without any contribution from Coconino sandstone at depths below Kaibab. The Coconino Formation is commonly assumed to be the major source of SiO₂ for the impact melts. Detailed trace element studies and associated mixing calculations must verify the absence of Coconino in the melts, work that is currently in progress. If correct, the major melt zone could be placed into the upper half of the excavated strata at Meteor Crater, a major finding not duplicated at any other crater.

Acknowledgements-Special thanks to Tom See, D.C. Golden, Charlie Galindo, Gerald Haynes, and Bill Davidson for taking time from their busy schedules to help when needed.

References:

- [1] Phinney W.C. and Simonds C.H. (1977) *Impact and Explosion Cratering*, Pergamon Press (NY), 771-790. [2] Grieve, R.A.F. *et al.* (1977) *Impact and Explosion Cratering*, Pergamon Press (NY), 791-814. [3] See, T.H. *et al.* (1998) *Meteoritics and Planetary Science* 33, 937-948. [4] See, T.H. *et al.* (1999) *LPSC XXX* abstract. [5] Shoemaker, E.M. and Kieffer, S.W. (1974) *Guidebook to Meteor Crater*, Univ. AZ. Press. [6] Roddy, D.J. (1978) *Proc. Lunar Planet. Sci. Conf. 9th*, 3891-3930. [7] McKee, E.D. (1938) *The Environment and History of the Toroweal and Kaibab Formations*, Carnegie Institution of Washington.

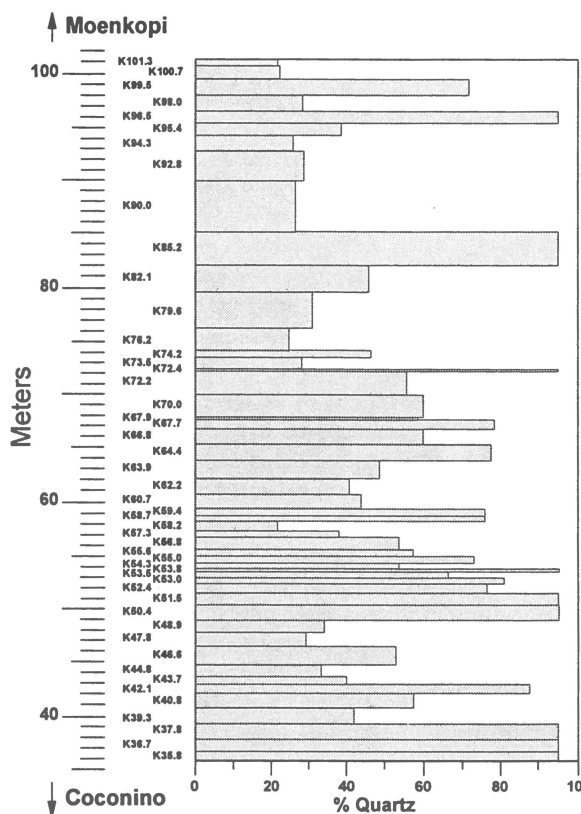


Figure 2. The percentage of quartz does not change systematically with increasing depth in the Kaibab Formation.

SEDIMENTARY DEPOSITS IN GANGIS CHASMA, MARS: STEREO AND GEOMORPHIC ANALYSIS

JENNIFER A. WAGGONER

South Dakota School of Mines & Technology, Rapid City, SD

ADVISOR: DR. ALLEN H. TREIMAN

Lunar and Planetary Institute, Houston, TX

INTRODUCTION

Valles Marineris is 4500 km long and located in the equatorial region of Mars. The parallel-sided canyons that constitute Valles Marineris formed as a result of major extensional (rift) faults in the fractured lithosphere surrounding the Tharsis uplift [1]. Unusual layered deposits on the floor on Valles Marineris were revealed during the Mariner 9 and Viking missions. Due to their rhythmic nature, great thickness, and lateral continuity, these deposits are important for understanding the depositional and erosional history of the canyon [2]. The origin of the layered deposits is a significant and outstanding question; they have been proposed to be either erosional remnants from the canyon wall, aeolian deposits, lacustrine material, or extrusive volcanic material [3].

Gangis Chasma is located south of Shalbatana Valles and north of Capri Chasma, and its layered deposit is located in the western part of the chasma at 7.4°S, 48.8°W. The deposit is about 110 km long (E-W) and 40-50 km wide with a maximum elevation of ~2.9 km. *Komatsu et al.* [2] identified a possible angular unconformity in Gangis where a dark layer appears tilted and truncated by overlying strata (Fig 1a). Using Viking Orbiter images I created a geomorphic map of Gangis Chasma, and using high-resolution Mariner 9 images I produced a digital topography model of the layered deposit. Topography data reveals that there is no angular unconformity in the Gangis layered deposit, rather a mantling deposit overlaps part of Tista layer (dark layer) giving the illusion that Tista is pinching out (Fig 1b).

METHODS

Viking and Mariner 9 images were processed from raw form through orthographic projections with ISIS and PICS image processing packages respectively. The digital topography model was constructed with the 'Z' macro to ISIS, developed by Dr. Paul Schenk (*Lunar and Planetary Institute*). Viking and Mariner 9 images were cosmetically adjusted with Adobe Photoshop. The geomorphic map of the Gangis Chasma layered deposits (Fig 1b) is based on Viking Orbiter images 610a13 and 897a40, which are both through red filters and at 0.204 km/pixel resolution. A digital topography model (Fig 2b) was developed using the stereo pair of

Mariner 9 images: m9_207b15 and m9_248b03. The two images of the same scene, taken from different positions, provide a three-dimensional view of the terrain in the same manner that two overlapping photographs are viewed through a stereoscope. These images were "tied" along the upper bench-layer to represent a datum (Fig 2a).

RESULTS

The terrain of Gangis Chasma is diverse in geologic features (Fig 1b). The canyon walls are about 2 km high with bifurcating and irregular spurs and gullies [1]. South of the layered deposits, on the canyon floor, are numerous mesas or hills that have a knob-like appearance. Their size generally decreases from east to west, ranging from 20 km wide to about 1 km wide. These may be eroded remnants of chaotic terrain or they could be volcanic constructs [4]. According to the Mars Global Surveyor (MGS) Mars Orbiter Camera (MOC) with resolutions in the 1.4 to 12 m/pixel range, the floor of Gangis Chasma is mantled with an extensive low relief "sand" sheet [5]. The sand sheet is located predominantly south of the layered deposits and in patches to the north and west. However, the floor of the canyon just north of the layered deposits is probably made up of landslide material from the canyon wall. This material is lighter in albedo compared to its neighboring sand sheet. In the northwestern part of the chasma there is an outspread, gently sloping deposit along the canyon wall closely resembling a terrestrial alluvial fan. Whether or not the material was deposited by fluvial processes is unknown. Fewer craters on the canyon floor than on the adjacent plateau suggests that the floor is younger, possibly as a result of erosional processes [6]. Two craters found in the dark material on the floor on the canyon, west of the layered deposits, are extremely eroded. The lack of impact ejecta indicates that the craters are very old and have been exhumed by weathering. Therefore, I and [4] interpret the surrounding dark material as an eroded older layer that has been exposed.

The main stratigraphic units of the layered deposits, determined by albedo, erosional morphology, and thickness, were given names: Brahmaputra layer, Tista layer, Gandak layer, and Yamuna layer (Fig 1b).

Overlying the Yamuna layer are several near-horizontal bench layers on the top of the mesa. To the west, the main units unconformably overlie the ancient cratered terrain mentioned above. As seen on the south-facing slope, the bottom three layers are conspicuously fluted, perhaps due to wind scouring or seepage of groundwater. The topography model (Fig 2b) reveals slope angles of 15° to 30° for Brahmaputra layer, 25° to 40° for Tista layer, 10° to 15° for Gandak layer, and 60° to vertical for Yamuna layer. On the eastern part of the south-facing slope are two lumps of material, each about 10 km wide. These lumps may be flatirons, or plates of steeply inclined resistant rock between deep valleys. On the other hand, their structure and fold-like texture suggest that they may be slumping material [2]. Running north-south down the slope of the layered deposits are lines of darker domes and ridges that may be volcanic domes and dikes intruded into the layered deposits and exposed by erosion. In addition, leaved channels of Brahmaputra layer imply processes of groundwater seepage within the deposit. A mantling deposit, smoother than the fluted area, gives Tista layer the illusion of pinching out. This region could be pyroclastic material- suggesting recent volcanism, yet it could also be a wedge of windblown sand or dust. According to elevation data, Tista layer does not tilt upward and truncate with the upper layers as [2] suggested; rather, it is flat (within a few degrees), as are the other layers.

CONCLUSION

I will consider four hypotheses for the origin of the Gangis Chasma layered deposits: erosional remnants from the canyon wall, aeolian deposits, lacustrine material, or extrusive volcanic material. **Erosional remnants from the canyon wall.** The morphology of the layered mesa material suggest that it is different from the surrounding canyon wall rock because no landslides are observed around the mesa walls and fine parallel fluting is observed on the mesa instead of the spur and gully morphology of the canyon wall [3]. **Aeolian deposits.** It was suggested that the layered terrains could be explained by global dust storms, but the deposits are only found inside the canyons and not on the plateau or the canyon walls [6]. **Lacustrine material.** Deposition within a low-energy, liquid-water environment could readily explain the horizontal bedding and lateral continuity of individual layers and their differences in reflectance and competence [3]. There is ample evidence that, at the time of canyon formation, substantial subsurface aquifers may have provided large quantities of water [6]. Perhaps water partially filled deep tectonic depressions and became capped in a thick cover of ice in the cold climate. Although deposition in standing water might account for the characteristics of the layers,

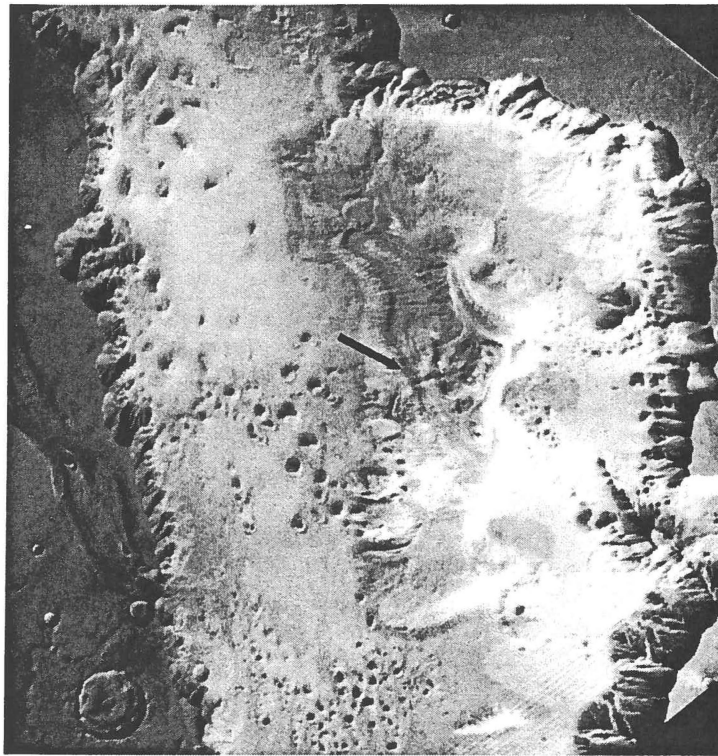
the source and composition of the material is an open question. In addition, the moat that surrounds the deposit is unexplained [3]. **Volcanic material.** The fluting visible along the edges of the layered deposits is similar to the fluting seen in terrestrial ignimbrites. Weitz [7] proposed that the layers in Hebes Chasma are in fact pyroclastic deposits. The sources for the deposits were fissures along the canyon floor that formed in association to rifting, yet they are now buried by younger layers or by mass wasting of wall rock. However, if this is the case, one would expect the layers to appear thicker near the source of the vent and thin away from it. On the other hand, if the volcanism were subaqueous, several arguments would be eliminated: material would be provided to an ice-covered lake without needing to penetrate or remove the ice cover, a subaqueous environment would more efficiently distribute material than a subaerial one, the interaction of magma and water may confine the flow to the interior of the canyon, and the material is more consistent with the lack of deposition on the surrounding plateau [3].

Because the leaved channels denote groundwater within the layered deposit, I'm inclined to support either the lacustrine or the subaqueous volcanism hypothesis. The presence of domes and ridges indicate intrusive volcanic activity after the deposition of these layers. Because the layers are not tilted as originally thought, there has been little tectonic activity since deposition. The draining, or evaporation, of the lake caused groundwater seepage, resulting in fluvial erosion and the formation of leaved channels along the slope. It is important to note that no rockfalls or talus cones are seen on the slopes, and the higher layers have extremely large slope angles, suggesting that the slopes have not been subject to degradative weathering.

Acknowledgments: This work would not have been possible without assistance from P. Schenk and B. Fessler. We also thank L. Wooley and D. Reub for technical help.

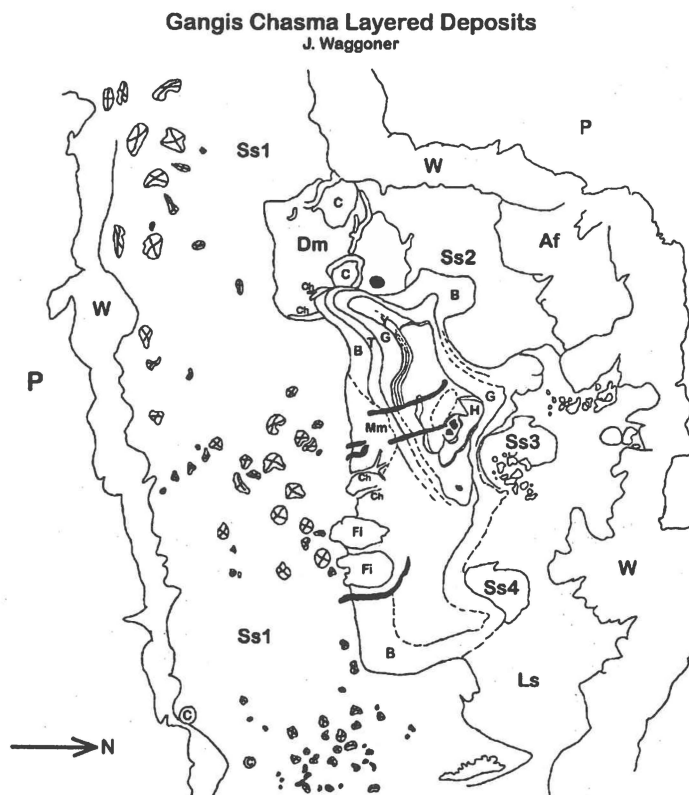
REFERENCES

- [1] Lucchitta, B. K., N. K. Isbell, and A. Howington-Kraus, *J. Geophys. Res.*, 99, 3783-3798, 1994; [2] Komatsu, G., P. E. Geissler, R. G. Strom, and R. B. Singer, *J. Geophys. Res.*, 98, 11105-11121, 1993; [3] Nedell, S. S., S. W. Squyres, and D. W. Anderson, *Icarus*, 70, 409-441, 1987; [4] Komatsu, G., and R. G. Strom, *LPSC XXI*, 651-652, 1990; [5] Edgett, K. S., Gangis Chasma Landing Site, unpublished, 1999; [6] Lucchitta, B. K., A. S. McEwen, G. D. Clow, P. E. Geissler, R. B. Singer, R. A. Schultz, and S. W. Squyres, Mars, *U. of Az. Press*, 453-492, 1992; [7] Weitz, C. M., *LPSC XXX*, Abstr. #1277, 1999.



⇐ **Figure 1.** a) Viking Orbiter image 610a13 of Gangis Chasma. Arrow points to the dark Tista layer that Komatsu *et al.* [2] claimed to be tilted and truncated by overlying strata, forming an angular unconformity. However, topography data indicates that this layer does not tilt and pinch out as originally believed.

b) Geomorphic map of the Gangis Chasma developed from Viking images 610a13 and 897a40.



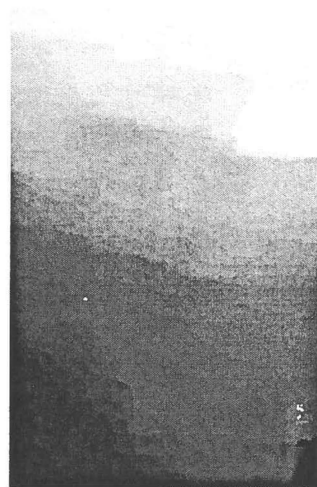
Geomorphic Units

- P plateau
- W wall rock
- Ss sand sheet (1, 2, 3, 4)
- Ls landslide material from canyon wall
- Dm dark material
- Af possible alluvial fan
- ⊗ mesa or hill
- ⊙ crater

Layered Deposits

- B Brahmaputra layer (bottom)
- T Tista layer (dark layer on image)
- G Gandak layer
- Y Yamuna layer (top 3 units)
- H near-horizontal bench layers
- Fi flatiron or slumping material
- Mm mantling material
- Ch leveed channel
- ▬ dome or ridge

20.4 km



↑ **Figure 2.** a) Mariner 9 image (m9_207b15) of Gangis Chasma. The ridge indicated by the arrow is the datum used for stereo imaging. b) Topography model generated from the stereo pairs. Lighter area shows greater elevation, and darker area shows lower elevation.

THE SEARCH FOR EXTRASOLAR PLANETS: A NEW APPROACH USING A GENETIC ALGORITHM

Danielle L. Wilhelmi, *Michigan State University, East Lansing, MI*

Advisors: Dr. David C. Black, *Lunar and Planetary Institute, Houston, TX*

Dr. Tomasz F. Stepinski, *Lunar and Planetary Institute, Houston, TX*

I. INTRODUCTION

Detecting extrasolar planets has proved to be difficult. Rather than looking for planets directly, several research groups are inferring their presence from the "wobble" of a star's apparent motion [1]. A gravitationally bound planet will swing its star around in a small mirror image of its own orbit, as they both move around the system's center of mass. The stellar wobbles are so small that the best way to detect them is to observe the Doppler effect they impose on a star's light.

Time series data of Doppler shift measurements are converted to radial velocities, which are the apparent motions of the star toward and away from the Earth. Plotting these velocities as a function of time will produce a radial velocity curve. Figure 1 shows the residual velocity data for the newly discovered Upsilon Andromedae system.

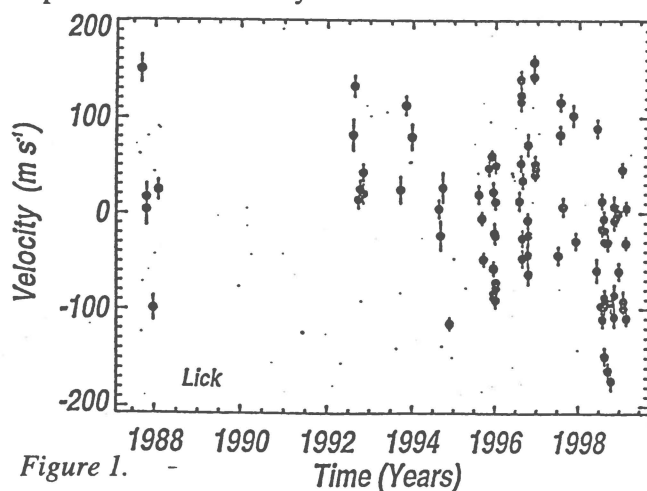


Figure 1.

Residual velocity is the velocity that's left over after the motion of the system through space is subtracted. The data is then modeled using Keplerian orbital mechanics to determine values for the five parameters of a Keplerian orbit: period, amplitude, eccentricity, periastron passage, and phase omega.

The first evidence of a possible multiple planet system has been discovered independently by two teams of astronomers [2]. This system lies 44 light-years away around the Sun-like star Upsilon Andromedae. The innermost planet was discovered in January of 1997 [3]. Upsilon Andromedae is the first candidate for an extrasolar planetary system.

The actual parameters of a companion's orbit are all defined by the curve that gives the "best fit" to the data. The "best fit" found by Butler *et al.* [2] indicates that the system has three companions. Their orbital parameters are given in Table 1. The periods are given in days, the amplitude in meters per second and the time of periastron passage in Julian days.

Companion b

Period	K	Ecc	Tperi	Omega
4.6171	74.5	0.042	10315.34	0.27925

Companion c

Period	K	Ecc	Tperi	Omega
242	56	0.23	11131.46	4.55531

Companion d

Period	K	Ecc	Tperi	Omega
1269	69.5	0.36	13813.24	4.11898

Table 1. Parameters of the companions in the Upsilon Andromedae system.

The purpose of this study is to investigate the validity of the three-companion system and check the parameters determined by Butler *et al.*

A genetic algorithm is used to approach this problem. The genetic algorithm is modeled after the evolution of a species where the fittest of the population survive to be part of and produce the next generation [4]. An advantage to using a genetic algorithm is that the standard method,

gradient based approach, introduce some bias because one must choose starting values, whereas the genetic algorithm randomly chooses values therefore no bias is introduced.

II. PROCEDURE

When fitting a model to observational data, a minimum is found using the χ^2 to give a fit to the data. The standard approach to determining the "best fit" is to use calculus to minimize the function because finding a minimum will give a "good fit" to the data. This approach will find a minimum, but it will most likely be only a local and not a global minimum. The words "best fit" imply that there is more than one solution and that all solutions are not of equal value. In fact, there may be several local minima and therefore many fits to the data, but there is only one global minimum. To ensure a "best fit" to the data a global minimum must be found. The challenge lies in finding the global minimum.

A new approach is to use a form of programming known as genetic algorithm because it has a higher probability of finding the global minimum of a function. Mathematica was used to write the algorithm [5]. The algorithm searches over a range of possible values for the parameters.

The algorithm randomly selects values for the parameters over a specified range to become the initial population. A large initial population provides the genetic algorithm with a large sample to search over. The initial population is too large to go through all the iterations performed by the genetic algorithm. Thus, a large portion of the population must be discarded through natural selection or survival of the fittest. Natural selection occurs with each iteration of the algorithm. Of the population, only the fittest survive for mating and the least fit are discarded to make room for the new offspring. Deciding how many to keep is somewhat arbitrary. Letting only a few survive to the next generation limits the available parameters in the offspring whereas, keeping too many allows the least fit a chance to contribute their traits to the next generation.

A mating pool is constructed consisting of the "fittest" of the population. Pairs of parents were chosen from the mating pool in such a way that it is most probable to select the fittest

individual over the least fit. Each mother/father pair produces two offspring and consequently, the offspring contain genes from both parents. The offspring then replace the bottom half of the population and become the next generation with their parents.

The genetic makeup of the population is limited to the current members of the population and helps the genetic algorithm to converge on a minimum value. Mutation occurs to introduce traits that were not present in the initial population and keeps the genetic algorithm from converging too quickly. The mutation rate determines how many mutations will occur. Increasing the number of mutations increases the algorithm's freedom to search outside the region specified by the initial population.

The population is then re-sorted so that the fittest are again on top, and the mating pool is selected and the whole cycle is reiterated until the specified number of generations has been reached.

III. RESULTS

In the algorithm used for this project, 100 individuals (ie, 100 sets of parameters) were selected to remain in the population from an initial population of 300. From this, 50 were selected to be a part of the mating pool. A mutation rate of 5% was used in all cases. Therefore, five mutations occurred in each iteration.

The algorithm was set up to run for 1000 generations. It ran three times for two different sets of possible ranges for the parameters. The first range was set close to the parameters found by Butler *et al.* to see if it would find a similar solution to theirs. The values for the parameters found by the algorithm are similar to those found by Butler *et al.* The second range was set a bit larger to see if another, possibly "better fit" could be found. The closest fit to their parameters is shown in Table 2 along with the average values of all the runs.

The program ran for 1000 generations and perhaps if it was run for more generations, then a better solution could be found. In addition, increasing the size of the population may enable a better solution to be found.

In the first six trials, the period of the first companion was assumed 4.6171 days because it

Run	Fitness	Companion b					Companion c					Companion d				
		P	K	Ecc	Tperri	Omega	P	K	Ecc	Tperri	Omega	P	K	Ecc	Tperri	Omega
Butler <i>et al.</i>	317.954	4.617	74.5	0.042	10315.34	0.27925	242	56	0.23	11131.46	4.55531	1269	69.5	0.36	13813.24	4.11898
closest	408.319	4.617	70.17	0.289	37.33	5.9981	238.437	44.33	0.4916	7072.58	4.52004	1269.22	60.86	0.2167	11092.6	3.03026
avg (1-3)	460.531	4.617	69.79	0.161	4819.42	2.271049	236.099	42.18	0.41	4139.79	4.26033	1265.25	60.96	0.075	9499.04	1.483816
avg (4-6)	724.02	4.617	72	0.073	2908.83	3.482341	1464.31	69.21	0.5699	6966.91	2.650696	1012.54	38.2	0.2649	4511.03	3.211207
avg (7-9)	2757.31	28.61	51.27	0.084	5142.53	5.73146	238.976	54.13	0.0123	7101.43	5.27319	1299.85	57.95	0.0089	10875.3	2.115795
avg (10-12)	2500.04	1.033	42.03	0.007	2205.79	3.706217	231.451	60.69	0.2016	3898.51	3.429753	1276	54.62	0.2628	33.5113	4.931

Table 2.

is so clearly defined. This left the algorithm 14 parameters to solve for. In trials seven through twelve, the algorithm solved for all 15 parameters.

IV. CONCLUSIONS

The genetic algorithm proved that the solution found by the Butler *et al.* is a fit for the data. It does *appear* to be the "best fit." However, further testing may reveal a more

appropriate set of parameters and thus the real "best fit."

V. REFERENCES

- [1] Black, D. C. (1999) *Encyclopedia of the Solar System*. 941-955. [2] Butler, R. P. et al (1999) submitted to ApJ. [3] Butler, R. P. and G. Marcy (1997) ApJ, 474, L115 [4] Haupt, R. L. and Haupt, S. E. (1998) *Practical Genetic Algorithms*. [5] Wolfram, S. (1996) *The Mathematica Book*.

